GRIFFITH UNIVERSITY

Dynamic characteristics of a sandy seabed under storm wave loading considering the effect of principal stress rotation

Author

Zhu, JF, Zhao, HY, Jeng, D-S

Published

2019

Journal Title

Engineering Geology

Version

Accepted Manuscript (AM)

DOI

10.1016/j.enggeo.2019.05.009

Rights statement

© 2019 Elsevier. Licensed under the Creative Commons Attribution-NonCommercial-NoDerivatives 4.0 International Licence (http://creativecommons.org/licenses/by-nc-nd/4.0/) which permits unrestricted, non-commercial use, distribution and reproduction in any medium, providing that the work is properly cited.

Downloaded from

http://hdl.handle.net/10072/387065

Griffith Research Online

https://research-repository.griffith.edu.au

Accepted Manuscript

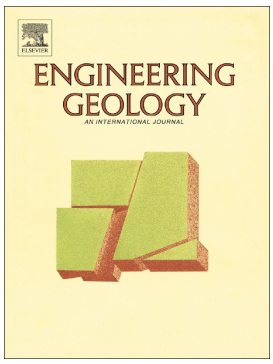

Dynamic characteristics of a sandy seabed under storm wave loading considering the effect of principal stress rotation

J.F. Zhu, H.Y. Zhao, D.-S. Jeng

PII: S0013-7952(18)31319-X
DOI: https://doi.org/10.1016/j.enggeo.2019.05.009
Reference: ENGEO 5132

To appear in: *Engineering Geology*

Received date: 4 August 2018
Revised date: 7 April 2019
Accepted date: 6 May 2019

Please cite this article as: J.F. Zhu, H.Y. Zhao and D.-S. Jeng, Dynamic characteristics of a sandy seabed under storm wave loading considering the effect of principal stress rotation, Engineering Geology, https://doi.org/10.1016/j.enggeo.2019.05.009

This is a PDF file of an unedited manuscript that has been accepted for publication. As a service to our customers we are providing this early version of the manuscript. The manuscript will undergo copyediting, typesetting, and review of the resulting proof before it is published in its final form. Please note that during the production process errors may be discovered which could affect the content, and all legal disclaimers that apply to the journal pertain.

ACCEPTED MANUSCRIPT

Dynamic characteristics of a sandy seabed under storm wave loading considering the effect of principal stress rotation

J.F. Zhu[a], H.Y. Zhao[b,c,*], D.-S. Jeng[c]

[a]Faculty of Architectural Civil Engineering and Environment, Ningbo University, Ningbo 315211, China

[b]College of Harbor, Coastal and Offshore Engineering, Hohai University, Nanjing 210098, China

[c]Griffith School of Engineering, Griffith University, Gold Coast Campus, QLD 4222, Australia

[*]Corresponding author.

ACCEPTED MANUSCRIPT

ACCEPTED MANUSCRIPT

ABSTRACT

This paper aims to investigate the cyclic characteristics of soil under storm waves with the typical irregular character, in which a generalized plasticity model considering the effect of principal stress rotation (PSR) was adopted to model soil behavior. In the present model, the plastic strain generated by principal stress rotation was considered to be an additional item in the constitutive relationship of soil, and the normalized loading and plastic flow directions were determined based on the stress tensor invariants. Comparisons between the present model, previous hollow cylinder apparatus (HCA) tests, and geotechnical centrifugal wave tests all show good agreement. Numerical results indicate that the moveable and random characteristics of the storm wave result in similar and irregular dynamic responses in sandy deposits along the extension direction of the seabed. Moreover, the severest wave loading in a real storm will significantly magnify both the speed and extent of liquefaction of the sandy seabed. Numerical results also demonstrate that ignoring the PSR involved in the storm–wave–seabed interaction will significantly underestimate the build-up of pore water pressure. Additionally, when considering the impact of PSR, the sandy seabed exhibits higher liquefaction resistance when subjected to the random wave compared to the representative regular wave. However, since the sharply weakening liquefaction resistance of soil under the severest wave condition cannot be captured with the regular wave, it is suggested that the random wave be adopted to further investigate the storm–wave–seabed interaction. Parametric studies show that soil properties (e.g., permeability and saturation) significantly affect the liquefaction characteristics of soil under storm waves.

Keywords: Storm; Random wave; Sandy seabed; Liquefaction; General plasticity theory; Principal stress rotation

ACCEPTED MANUSCRIPT

1. Introduction

Storms usually have moveable, variable, and irregular cyclic characteristics, which may result in cyclic plasticity (the tendency for contraction under cyclic loading), accumulation of pore pressure, and continuous principal stress rotation in soil deposits, further influencing the stability of the seabed near offshore structures. In fact, seabed liquefaction has become a key process responsible for geo-hazards in waterfronts associated with storm waves. For example, Christian et al. (1974) reported that a pipeline in Lake Ontario had failed several times during storms apparently due to liquefaction, while Herbich et al. (1984) also found that a pipeline under construction floated to the seabed surface after a severe storm. Miyamoto et al. (1989) reported the subsidence of offshore breakwaters on the Niagata Coast of Japan, which was later attributed to seabed liquefaction by Goda (1994). Ishihara and Yamazaki (1984) found that the liquefaction depth of a seabed with a water depth of 14 m could approach 17.7 m in several storms for a medium-dense deposit of sand with 70% relative density. Sassa et al. (2006) also observed that the residual pore water pressures could accumulate at various sand depths shallower than 2.0 m when the significant wave heights exceeded 2.0 m under the passage of storm waves. Consequently, it is important for marine geotechnical and coastal engineers to understand the physical process of wave-induced soil response and improve designs that can prevent or mitigate the possibility of damage caused by storm wave loading.

On the topic of wave–seabed interactions, a range of investigations involving laboratory experiments (Sassa and Sekiguchi 1999; Kirca et al. 2013; Xu et al. 2017), analytical approximations (Hsu and Jeng 1994; Jeng and Seymour 2007), and numerical modeling (Sassa et al. 2001; Zhao et al., 2017a; Zhao et al., 2017b; Chen et al., 2018; Guo et al., 2019;

ACCEPTED MANUSCRIPT

Li et al., 2019) have been reported in the literature to date. However, most of these studies are restricted to regular and periodic waves and the results obtained may not be directly applicable to real coastal conditions, i.e. in a storm in which waves are irregular and random as shown in Fig. 1. Based on undrained cyclic triaxial tests, Pan and Yang (2018) reported that the build-up of the pore water pressure and liquefaction potential of sand is significantly influenced by the irregularity of the random wave. Moreover, as accident rates due to geotechnical and structural deficiencies remain comparatively high (Hunt and Marsh 2004), there is strong impetus to understand their behavior under realistic loading conditions.

During storms, the actual cyclic loading is normally irregular with continuous variation in cyclic amplitude. Thus, it can be modeled by adopting spectral analyses such as B-M spectrum (Bretschneider, 1968; Mitsuyasu, 1970), JONSWAP spectrum (Hasselmann et al. 1973) or P-M spectrum (Pierson and Moskowit 1964), as discussed by Franco et al. (1998). Liu and Jeng (2007) presented a semi-analytical solution to investigate the random wave-induced soil response in marine sediments with a finite soil thickness. In this solution, the random waves were generated on the basis of the two typical frequency spectra, BM spectrum and JONSWAP spectrum, and the soil response was described by the elastic model. It was found that for the same saturation, the maximum liquefaction depth induced by the random wave was much larger than that induced by the corresponding representative regular waves. Similarly, Zhou et al. (2014) also compared the soil response under different wave loading (random wave, Stokes wave, and cnoidal wave), treating the seabed as a poro-elastic medium. However, the typical soil response under storm waves such as cyclic plasticity, accumulation of residual pore pressure, and the principal stress rotation effect cannot be

ACCEPTED MANUSCRIPT

reproduced by the elastic model. Therefore, it is necessary to adopt poro-elastoplastic models to address the above responses of a sandy seabed under storm wave loading.

To investigate the wave-induced soil response within the frame of poro-elastoplastic theory, three key issues should be considered, as discussed by Pastor et al. (1999): a non-associative flow rule, a hardening law not only dependent on the soil density, and the possibility of plastic strains upon unloading. The model Pastor–Zienkiewicz Model Mark-III (PZIII) (Pastor et al. 1990), offers a convenient framework for the consideration of such issues. In this model, the yield and plastic potential surfaces do not need to be defined explicitly. Instead, the direction vectors are incorporated and the computational efficiency is significantly improved in the finite element method (FEM) as the stress point does not have to be brought back to the yield surface, which is the case in the traditional elastoplastic model (Zienkiewicz et al. 1998). Recently, the PZIII has been successfully employed to describe the cyclic behaviors of sand such as liquefaction and cyclic mobility due to earthquake loading, wave loading (Jeng and Ou 2010; Ye et al. 2015). Recently, Zhang et al. (2013) modeled the seabed response around breakwater heads under random wave loading. Unfortunately, the continuous rotation of the principal stress due to cyclic wave loading cannot be captured by the original PZIII model as stated by Zhang et al. (2013), because of the assumption of pure principal stress rotation without changing the amplitude of cyclic deviatoric stress, thus having no contribution to plastic strains.

In general, the deformation characteristics of soil deposits are closely related to the changes in both the direction and magnitude of the principal stress and may in fact be purely related to the principal stress rotation (PSR) even without a change in principal stress

ACCEPTED MANUSCRIPT

magnitudes under wave loadings (Ishihara and Towhata 1983). Continuous PSR can also generate excess pore water pressure and cumulative shear strain when the drainage condition is impeded (Yang et al. 2007; Qian et al. 2016; Wang et al. 2017a). This has been a subject of concern for clarification of the liquefaction mechanisms around marine structures (Ye et al. 2015). Ignoring PSR-induced deformation may lead to unsafe or even contradictory design in the practice of ocean engineering. Based on the generalized plasticity theory, Sassa and Sekiguchi (2001) proposed a modified version of PZIII by considering the effects of principal stress orientation in which the loading functions, plastic potential functions, and plastic modulus were defined with a new major principal stress angle parameter ψ. However, Sassa and Sekiguchi's model (Sassa and Sekiguchi 2001) only considers two-dimensional mean effective stress and the maximum shear stress as stress variables while neglecting out-of-plane stress, despite its importance for determining plastic flow conditions (Perić and Ayari 2002). Moreover, the major principal stress angle ψ is not a stress tensor invariant, so it may not be reasonable for Sassa and Sekiguchi (2001) to consider the effect of principal stress rotation by taking the derivative of the plastic flow and loading function with respect to ψ.

This study aims to investigate the soil response under irregular cyclic loadings, particularly the storm–wave loading, in which the impact of PSR is considered in the numerical simulations of random wave–seabed interactions using a modified plasticity soil model (modified PZIII). Unlike previous works (Sassa and Sekiguchi 2001), the PSR-induced soil deformation is considered in the simulation by treating it as an independent source of the plastic strain rate (Li et al. 2011) and establishing the relationship of the

ACCEPTED MANUSCRIPT

normalized loading direction and plastic flow direction with only the stress tensor invariants. The developed model is validated through comparison with the simulated and tested results from HCA elementary tests (Towhata and Ishihara 1985) and the geotechnical centrifugal wave tests (Sassa and Sekiguchi 1999). Then, the JONSWAP spectrum is utilized to generate the random waves under real storm conditions (Franco et al. 1998). By adopting the proposed model, the effects of PSR on the liquefaction susceptibility of a sandy seabed under random waves are investigated and compared with the results from the original PZIII model. The difference in the cyclic characteristics of soil under the random wave and representative regular wave loading considering the impact of PSR is also investigated. Finally, the sensitivity of wave-induced soil liquefaction to permeability and saturation of soil is analyzed through parametric studies.

2. Governing Equations - *u-p* Approximation

In general, geo-materials selected as foundations for coastal and offshore structures are inherently heterogeneous, basically consisting of two phases: a solid phase with soil skeleton and a fluid phase with water and air. Each phase has a different state of motions, leading to interactions between them. To better understand the mechanism of sea-floor dynamics under wave loading, an appropriate mathematical modeling of soil skeleton–pore fluid interaction is of paramount importance (Jeng 2003). In this study, a geotechnical model for the wave–seabed interaction is developed in two-dimensions under plane strain idealization, in which Biot's "*u-p*" approximation (Biot 1956) is used for linking the solid–pore fluid interaction in the porous seabed. This is described by Eqs. (1) to (3):

ACCEPTED MANUSCRIPT

$$\frac{\partial \sigma'_x}{\partial x} + \frac{\partial \tau_{xz}}{\partial z} = -\frac{\partial p_e}{\partial x} + \rho \frac{\partial^2 u_s}{\partial t^2} \quad (1)$$

$$\frac{\partial \tau_{xz}}{\partial x} + \frac{\partial \sigma'_z}{\partial z} + \rho b_g = -\frac{\partial p_e}{\partial x} + \rho \frac{\partial^2 w_s}{\partial t^2} \quad (2)$$

$$k_s \nabla^2 p_e - \gamma_w n_s \beta_s \frac{\partial p_e}{\partial t} + k_s \rho_f \frac{\partial^2 \varepsilon_v}{\partial t^2} = \gamma_w \frac{\partial \varepsilon_v}{\partial t} \quad (3)$$

where p_e is the wave-induced excess pore pressure; ∇^2 is the Laplace operator; ns is the porosity of soil; b_g is the gravitational acceleration; k_s is Darcy's permeability coefficient; σ'_x and σ'_z are the horizontal and vertical components of effective normal stresses, respectively; τ_{xz} is the shear stress; γ_w is the unit weight of pore fluid; ρ (= $\rho_f n_s + \rho_s(1-n_s)$) is the average density of porous seabed, where ρ_f is the fluid density and ρ_s is the solid density; and u_s and w_s are soil displacements in the x- and z-directions, respectively. The volume strain of soil matrix ε_v and compressibility of the pore fluid β_s can be defined as

$$n_s = \left(\frac{1}{K_w} + \frac{1-S_r}{p_{w0}}\right), \ \varepsilon_v = \frac{\partial u_s}{\partial x} + \frac{\partial w_s}{\partial z} \quad (4)$$

where K_w is the true bulk modulus of elasticity of water; p_{w0} is the absolute water pressure; and S_r is the degree of saturation.

The model is developed using the finite element code *DIANA-SWANDYNE II*, in which the displacement $\boldsymbol{u}$ (u_s, w_s) and pore pressure $\boldsymbol{p}$ (p_e) in Eqs. (1) to (3) are chosen as the two field variables and can be solved simultaneously using FEM. The implicit scheme GNpj (Generalized Newmark p-th order scheme for j-th order equation) is used for the time integration scheme, in which all quantities are defined at a discrete time station when solving the above governing equations (Chan 1995). In each time step, the increments of the effective stress $d\boldsymbol{\sigma}' = [d\sigma'_x, d\sigma'_z, d\tau_{xz}]$were computed from an appropriate constitutive model, either elastic or elastoplastic, as follows:

ACCEPTED MANUSCRIPT

$$d\boldsymbol{\sigma}' = \boldsymbol{D}d\boldsymbol{\varepsilon} = \boldsymbol{D}\begin{bmatrix} d\varepsilon_x \\ d\varepsilon_z \\ d\varepsilon_{xz} \end{bmatrix} = \boldsymbol{D}\begin{bmatrix} \frac{\partial u_s}{\partial x} \\ \frac{\partial w_s}{\partial z} \\ \frac{1}{2}\left(\frac{\partial u_s}{\partial z} + \frac{\partial w_s}{\partial x}\right) \end{bmatrix} \quad (5)$$

where $d\varepsilon_x$, $d\varepsilon_z$, and $d\varepsilon_{xz}$ are the three components of the strain on soil and $\boldsymbol{D}$ is the elastic or elastoplastic matrix (depending on the constitutive model used). Further information about discretization in the space and time domains can be found in Zienkiewciz et al. (1998).

Since a sandy seabed will become increasingly dense when subjected to long-term wave loading, in each time step the void ratio (e) and corresponding permeability coefficient (k_s) of seabed soil are assumed to be modified as follows (Miyamoto and Sassa 2004):

$$e_{n+1} = (1 + e_n)\exp(\beta_s \Delta p + \Delta\varepsilon_v) - 1,\ k_{sn+1} = k_{s0}\frac{e_0^3}{1+e_0}\frac{e_{n+1}^3}{1+e_{n+1}} \quad (6)$$

where e_{n+1} and e_n are void ratios at the (n+1)-th and n-th time steps, respectively; $\Delta\varepsilon_v$ is the incremental volume strain of soil; Δp is the incremental pore water pressure; k_{sn+1} and k_{s0} are the permeability coefficients of seabed soil at the (n+1)-th time step and the initial condition, respectively; and e_0 is the initial void ratio.

3. Boundary Condition

To solve the boundary value problem involved in random wave-seabed interactions as shown in Fig. 1, the following initial and boundary conditions are set:

(a) both lateral sea side boundaries of the seabed are fixed in the horizontal direction.

(b) zero soil displacement are assumed for the soil resting on an impermeable rigid base, and pore water pressure is applied with zero-gradient boundary conditions.

(c) at the mudline, the pore water pressure is equal to the wave-induced dynamic water pressure with no soil displacement constraints.

ACCEPTED MANUSCRIPT

4. Constitutive Model

4.1. Modified PZIII Model with PSR

The PZIII model was originally developed by Zienkiewicz et al. (1998) and Pastor et al. (1990) based on the generalized plasticity theory, in which the loading and plastic flow directions can be directly defined on the basis of the experimental findings without showing any explicit yield and plastic potential surface. In addition, the PZIII model can simulate stress-strain response in different initial conditions under monotonic and cyclic loading. Recently, this model has been widely used for reproducing the liquefaction characteristics of a seabed under cyclic waves with satisfactory results (Ye et al. 2015). However, the PSR-induced deformation cannot be reproduced using the original PZIII model, which may lead to unsafe design in practical engineering. Therefore, Sassa and Sekiguchi (2001) extended the PZIII model by considering the loading function, the plastic potential function, and the plastic modulus to be related to the major principal stress angle ψ (as shown in Fig. 2):

$$\psi = \frac{1}{2}\tan^{-1}[2\tau_{xz}/(\sigma'_z - \sigma'_x)] \quad (7)$$

However, the major principal stress angle ψ is not a stress tensor invariant. Therefore, it may not be reasonable to consider the effect of the principle stress axes rotation like Sassa and Sekiguchi's model (Sassa and Sekiguchi 2001). Sassa and Sekiguchi's model did not consider the effect of the out-of-plane stress σ'_y, despite its importance in determining the plastic flow direction. Furthermore, it is inappropriate to consider the major principal stress angle (ψ) as a stress tensor invariant in the model (Sassa and Sekiguchi 2001).

ACCEPTED MANUSCRIPT

A general formulation for modeling the total strain rate can be written as follows (Li et al. 2011):

$$d\boldsymbol{\varepsilon} = d\boldsymbol{\varepsilon}_e + d\boldsymbol{\varepsilon}_p = \boldsymbol{D}_e^{-1} d\boldsymbol{\sigma}' + \frac{(\boldsymbol{n}_g \otimes \boldsymbol{n})}{H_L} d\boldsymbol{\sigma}' + \frac{\boldsymbol{n}_g dX}{H_X} \quad (8)$$

where $d\boldsymbol{\varepsilon}_e$ is the elastic strain rate vector; $d\boldsymbol{\varepsilon}_p$ is the plastic strain rate vector; $\boldsymbol{D}_e$ is the elastic stiffness tensor; $\boldsymbol{n}_g$ is the normalized plastic flow direction vector; $\boldsymbol{n}$ is the normalized loading direction vector; H_L is the plastic modulus; and H_X controls the shrinkage of the yield surface caused by changes in X, which can be substituted with suction, temperature, or other factors to meet a variety of needs in practical application.

Let $dX = \chi d\psi = (\chi\, \partial\psi/\partial\sigma')d\sigma'$ and H_L=H_ψ, then

$$d\boldsymbol{\varepsilon} = \boldsymbol{D}_e^{-1} : d\boldsymbol{\sigma}' + \frac{\left(\boldsymbol{n}_g \otimes (\boldsymbol{n} + \chi \partial\psi/\partial\sigma')\right)}{H_\psi} \quad (9)$$

where χ is a parameter dependent on whether the effect of PSR is considered $\begin{cases} a = b = 0, & \chi = 0 \\ \text{other cases}, & \chi = 1 \end{cases}$; H_ψ is the plastic modulus considering the effect of PSR; and the subscript ψ presents the major principal stress angle.

Symes et al. (1984) conducted a series of undrained monotonic torsion shear tests on identical specimens of medium-loose sand. The test results show that the principal stress angle ψ significantly affects the contractive behavior and the main physical parameters such as the plastic potential function g, the loading function f and the plastic modulus H_L. With an increase in ψ, decreases in p' and q_p are associated with a remarkable drop in the phase transformation line. Then, the normalized plastic flow direction tensor (m_{ij}) and loading direction tensor (n_{ij}) can be accordingly defined for plastic flow direction as follows: $m_{ij} = \frac{\frac{\partial g}{\partial \sigma'_{ij}}}{\left\|\frac{\partial g}{\partial \boldsymbol{\sigma}'}\right\|} = \frac{\frac{\partial g}{\partial p'}\frac{\partial p'}{\partial \sigma'_{ij}} + \frac{\partial g}{\partial q}\frac{\partial q}{\partial \sigma'_{ij}} + \frac{\partial g}{\partial \theta}\frac{\partial \theta}{\partial \sigma'_{ij}}}{\left\|\frac{\partial g}{\partial p'}\frac{\partial p}{\partial \boldsymbol{\sigma}'} + \frac{\partial g}{\partial q}\frac{\partial q}{\partial \boldsymbol{\sigma}'} + \frac{\partial g}{\partial \theta}\frac{\partial \theta}{\partial \boldsymbol{\sigma}'}\right\|}$ (10)

ACCEPTED MANUSCRIPT

where

$$\frac{\partial g}{\partial p'} = [1 + \alpha(\psi)]\left[M_g(\psi) - q/p'\right], \quad \frac{\partial g}{\partial q} = 1, \quad \frac{\partial g}{\partial \theta} = -\frac{q}{2} M_g(\psi)\cos 3\theta \tag{11}$$

The parameters $M_g(\psi)$, $M_f(\psi)$, $\alpha(\psi)$, and $U(\psi)$ can be written as (Sassa and Sekiguchi 2001)

$$M_g(\psi) = M_{g0} - U(\psi) \cdot a \cdot M_{g0}, \quad M_f(\psi) = M_{f0} - U(\psi) \cdot a \cdot M_{g0} \tag{12}$$

$$\alpha(\psi) = \alpha_0 + b \cdot U(\psi) \tag{13}$$

$$U(\psi) = \begin{cases} 1 - \cos(2\psi) & 0 \le \psi \le \pi/4 \\ 1 - \cos(2|\psi|) & \pi/4 \le \psi \le \pi/2 \end{cases} \tag{14}$$

where

$$p' = \left(\sigma'_x + \sigma'_y + \sigma'_z\right)/3 \tag{15}$$

$$q = \frac{1}{\sqrt{2}}\sqrt{\left(\sigma'_x - \sigma'_y\right)^2 + \left(\sigma'_y - \sigma'_z\right)^2 + (\sigma'_z - \sigma'_x)^2 + 6\tau_{xz}^2} = \sqrt{3J_2} \tag{16}$$

$$\sin 3\theta = \frac{-3\sqrt{3}}{2}\frac{J_3}{(J_2)^{\frac{3}{2}}} = -\frac{\sqrt{27}J_3}{2q^3} \tag{17}$$

$$J_3 = \frac{1}{\sqrt{2}}(\sigma'_x - p')\left(\sigma'_y - p'\right)(\sigma'_z - p') - \left(\sigma'_y - p'\right)\tau_{xz}^2 \tag{18}$$

Here p' is the mean effective stress; q is the generalized shear stress; θ is the Lode angle; I_1, J_2, J_3 are the first, second, and third deviatoric stress tensor invariants, respectively; $\alpha(\psi)$ is the coefficient related to the stress-dilatancy relationship of soil; $M_g(\psi)$ is the slope of the phase transformation line; $M_f(\psi)$ is the material parameter that determines the size of the loading surface ; a and b are constants associated with $M_g(\psi)$ and $\alpha(\psi)$, respectively; M_{g0} and M_{f0} are $M_g(\psi)$ and $M_f(\psi)$ for ψ =0, respectively; and $\alpha_0 = \alpha$ for ψ = 0. The parameters p', q, and θ are also stress tensor invariants since they are functions of I_1, J_2, and J_3, respectively.

M_{g0} and M_{f0} in Eq. (11) can be determined as follows:

$$M_{g0} = \frac{6\sin\varphi_{g0}}{3 - \sin\varphi_{g0}\sin 3\theta}, \quad M_{f0} = \frac{6\sin\varphi_{f0}}{3 - \sin\varphi_{f0}\sin 3\theta} \tag{19}$$

where θ is the Lode angle as mentioned earlier; φ_{g0} is the residual frictional angle of sand

ACCEPTED MANUSCRIPT

when $\theta = 30^{\circ}$ in triaxial compression tests (Chang 1995; Zienkiewicz et al. 1998); and φ_{f0} is a parameter related to φ_{g0} and relative density D_r. Here, it is assumed that

$$\sin\varphi_{f0} = D_r \sin\varphi_{g0} \tag{20}$$

Then,

$$\frac{\partial g}{\partial \theta} = \frac{\partial g}{\partial M_g(\psi)} \cdot \frac{\partial M_g(\psi)}{\partial \theta} = -\frac{q}{2M_g(\psi)}\left[M_{g0}^2 - a \cdot U(\psi) \cdot M_{g0}^2\right]\cos 3\theta \tag{21}$$

for loading direction:

$$n_{ij} = \frac{\frac{\partial f}{\partial \sigma'_{ij}}}{\left\|\frac{\partial f}{\partial \boldsymbol{\sigma}'}\right\|} + \chi\frac{\partial \psi}{\partial \sigma'_{ij}} = \frac{\frac{\partial f}{\partial p'}\frac{\partial p'}{\partial \sigma'_{ij}} + \frac{\partial f}{\partial q}\frac{\partial q}{\partial \sigma'_{ij}} + \frac{\partial f}{\partial \theta}\frac{\partial \theta}{\partial \sigma'_{ij}}}{\left\|\frac{\partial f}{\partial p'}\frac{\partial p}{\partial \boldsymbol{\sigma}'} + \frac{\partial f}{\partial q}\frac{\partial q}{\partial \boldsymbol{\sigma}'} + \frac{\partial f}{\partial \theta}\frac{\partial \theta}{\partial \boldsymbol{\sigma}'}\right\|} + \chi\frac{\partial \psi}{\partial \sigma'_{ij}} \tag{22}$$

$$\frac{\partial f}{\partial p'} = [1 + \alpha(\psi)]\left[M_f(\psi) - q/p'\right], \quad \frac{\partial f}{\partial q} = 1, \quad \frac{\partial f}{\partial \theta} = -\frac{q}{2M_f(\psi)}\left[M_{f0}^2 - a \cdot U(\psi) \cdot M_{g0}^2\right]\cos 3\theta \tag{23}$$

Here, only the rotation in the x and z planes was considered, and the partial derivative $\frac{\partial \psi}{\partial \sigma'_{ij}}$ can be given as follows (Sassa and Sekiguchi 2001):

$$\frac{\partial \psi}{\partial \sigma'_x} = \frac{\tau_{xz}}{(\sigma'_x - \sigma'_z)^2 + \tau_{xz}^2}, \ \frac{\partial \psi}{\partial \sigma'_z} = \frac{-\tau_{zx}}{(\sigma'_x - \sigma'_z)^2 + \tau_{xz}^2}, \ \frac{\partial \psi}{\partial \sigma'_y} = 0, \ \frac{\partial \psi}{\partial \tau_{xz}} = \frac{(\sigma'_x - \sigma'_z)/2}{(\sigma'_x - \sigma'_z)^2 + \tau_{xz}^2} = \frac{\partial \psi}{\partial \tau_{zx}} \tag{24}$$

Based on the original PZIII model (Pastor et al. 1990) and Sassa and Sekiguchi's model (Sassa and Sekiguchi 2001), the plastic modulus H_ψ considering the effect of the principle stress rotation can be assumed to be

$$H_\psi = H_0 \cdot p'\left[1 - \frac{\eta(\psi)}{\eta_f^*}\right]^4 \cdot \left[\left[1 - \frac{q/p'}{M_g(\psi)}\right] + \beta_0\beta_1 \mathrm{e}^{-\beta_0\xi}\right] \tag{25}$$

$$\eta(\psi) = \frac{q}{p'} - [1 - U(\psi)] \cdot aM_{g0}, \quad \eta_f^* = \left(M_{f0} - aM_{g0}\right)(1 + 1/(\alpha_0 + b)) \tag{26}$$

where H_0 is a model parameter that scales the plastic modulus; β_0 and β_1 = material constants; and ξ is the accumulated deviatoric plastic strain; $\xi = \int |d\varepsilon_q^p|$.

The plastic modulus $H_{\psi u}$ for unloading can be assumed to be

ACCEPTED MANUSCRIPT

$$H_{\psi u} = \begin{cases} H_{\psi u0}\left[\frac{M_g(\psi)}{(q/p')_u}\right]^{\gamma_u} & \text{for } \left|\frac{M_g(\psi)}{(q/p')_u}\right| > 1 \\ H_{\psi u0} & \text{for } \left|\frac{M_g(\psi)}{(q/p')_u}\right| \le 1 \end{cases} \quad (27)$$

where $H_{\psi u0}$ is a material parameter that can be assumed as equal to H_0, and $(q/\ p')_u$ is the effective stress ratio at which unloading takes place. For the unloading process, the following modification is required (Pastor et al. 1990):

$$\frac{\partial g}{\partial p'} = -\left|\frac{\partial g}{\partial p'}\right| \quad (28)$$

where $\partial g/\partial q$ and $\partial g/\partial\theta$ are the same as Eq.(11).

Then, the constitutive relations may finally be expressed as follows:

$$d\sigma'_{ij} = \begin{cases} \left(D^e_{ijkl} - \frac{D^e_{ijmn}m_{mn}n_{st}D^e_{stkl}}{H_\psi + n_{st}D^e_{stkl}m_{kl}}\right)d\varepsilon_{kl} & \text{for loading} \\ \left(D^e_{ijkl} - \frac{D^e_{ijmn}m_{mn}n_{st}D^e_{stkl}}{H_{\psi u} + n_{st}D^e_{stkl}m_{kl}}\right)d\varepsilon_{kl} & \text{for unloading} \end{cases} \quad (29)$$

where D^e_{ijkl} is the elastic stiffness tensor for isotropic elasticity, that is,

$$D^e_{ijkl} = \lambda\delta_{ij}\delta_{kl} + 2G\delta_{ik}\delta_{jl}, \quad G = Gp'/p'_0, \ \lambda = 3K\upsilon/(1+\upsilon), \quad K = K_{ev0}p'/p'_0 \quad (30)$$

where G is the shear modulus that can be assumed to be dependent on the mean effective stress p'(Pastor et al. 1990); G_0 and p'_0 are the shear modulus and initial mean effective stress before shearing, respectively; δ is the Kronecker symbol; λ is Lame's constant; and K is the body modulus (the initial value is K_{ev0}).

There are thirteen parameters (φ_{g0}, a, b, α_0, β_0, β_1, γ_u, H_0, H_{U0}, K_{ev0} or G_{ev0}, υ and p'_0) in the proposed model. a, b, and α_0 are the most important to reflect the effects of PSR and can be calibrated by conducting the hollow torsional shear experiment suggested by Liu et al. (2015). β_0, β_1, γ_u, H_0, and H_{U0} can also be determined by fitting a monotonic stress–strain curve and conducting cyclic triaxial shear tests as suggested by Pastor et al. (1990). φ_{g0} can be obtained when $\theta = 30^\circ$ in triaxial compression tests, υ can be obtained from

ACCEPTED MANUSCRIPT

isotropic compression test, and K_{ev0} or G_{ev0} can be obtained from the stress–strain curve from triaxial tests with small strain measurement. Lastly, p'_0 is the initial mean effective stress before shearing in the undrained triaxial test (Zienkiewicz et al., 1998) In addition, D_r is the relative density of sand, which can be determined by the specific gravity of solid particles test.

4.2. Verification of the Model

4.2.1. HCA Element Test

An element test concerning the rotational orientation of the principal stress axis is performed to verify the reliability of using the present constitutive model to reproduce the effects of PSR. The model parameters as suggested by Sassa and Sekiguchi (2001) are listed in Table 1.

Towhata and Ishihara (1985) conducted a series of HCA tests to investigate the deformation characteristics of the sand under the condition of continuous principal stress rotation. The measured data used for verification of the present model was conducted following a semi-circle stress path, as shown in Fig. 3, in which the deviator stress $(\sigma'_1 - \sigma'_3)/2$ was held constant at 76.7 kPa and the direction of the major principal stress (ψ) rotated continuously with the orientation angle ranging from $-\pi/4$ to $\pi/4$. Fig. 4 shows the stress–strain relationship in the soil element subject to the drained shear test. The figure shows a comparison of the present model results with the HCA test results conducted by Towhata and Ishihara (1985). The results indicate that a pure principal stress rotation, even without changing the stress amplitude, can accelerate the development of volumetric strains. It is found that the simulated results are in good agreement with the measured data, indicating

ACCEPTED MANUSCRIPT

that PSR-induced deformation can be well-captured using the developed model.

4.2.2. Geotechnical Centrifuge Tests

Sassa and Sekiguchi (1999) carried out geotechnical centrifuge tests to understand the liquefaction characteristics of a sandy seabed under different types of waves, including progressive and standing waves. To verify the present model, the identical test case of Sassa and Sekiguchi (2001) will be reproduced in this section using the developed model. The simulated results including excess pore pressure, effective and deviatoric stress paths, and shear stress–strain response will be compared with the results of Sassa and Sekiguchi (2001).

In the centrifuge test (Sassa and Sekiguchi 1999), a bed of saturated, loose Leighton Buzzard sand was subjected to sinusoidal wave loading with one wave length (L_0=510 mm), one wave period (T=0.091 s). All wave tests were performed under a steady-state centrifugal acceleration of 50 g. The soil bed was 200 mm wide (W) and 100 mm deep (h). The side boundaries were set to be smooth and impermeable, and the bottom boundary was fixed and impermeable. The weight of soil, γ', was equal to 425 kN/m^3, the water depth was 90mm and the wave number, κ(=2π/L_0), was 12.2 m^{-1}.

First, a linear sinusoidal progressive wave is applied on the seabed as a pressure boundary condition with the following form:

$$\sigma'_z + p_e = p_b(x,0,t) = p_0 \cos(\kappa x - \omega t)\,, \tau_{xz} = 0, \quad at\ z = 0 \tag{31}$$

where p_b is the dynamic wave pressure at the seabed surface; p_0(=$\gamma_w H$/(2cosh κd)) is the amplitude of the wave pressure at the seabed surface; H is the wave height; d is the water depth; and $\omega = 2\pi/T$ is the angular frequency of the waves. The soil tension is assumed to be positive. The wave and soil parameters used in the validation are the same as those used by

ACCEPTED MANUSCRIPT

Sassa and Sekiguchi (2001), which are given in Table 2. The corresponding wave loading intensity p_0 and cyclic stress ratio $\chi_0 = \kappa p_0/\gamma'$ are 5.0 kPa and 0.14, respectively. As demonstrated by Jeng and Zhao (2015), there is no significant discrepancy in the horizontal distribution of pore pressure accumulation in the case of progressive waves. As an example, the responses of a soil element on the centerline with the centroid at z = 15 mm is taken as the representative location for verification. The measured values of $p_{\max}/(-\sigma'_{v0})$ and χ_0 for loose Leighton Buzzard sand under progressive wave loading in the centrifuge wave tank tests (Sassa and Sekiguchi 1999) are shown by the solid circles in Fig. 5 (x = 0, z = 15 mm). The predicted curves of both the present model and Sassa and Sekiguchi's model (Sassa and Sekiguchi 2001) are also plotted. It can be observed that the two simulated results are relatively consistent with the results of the centrifuge tests. The maximum of the residual pore pressure $p_{\max}$ shows s-shaped growth with the increase of the cyclic stress ratio χ_0. Until $\chi_0 \geq 0.14$, the ratio $p_{\max}/(-\sigma'_{v0})$ approaches to unity. This implies that liquefaction occurs as was observed in the centrifuge tests.

Additionally, Fig. 5 shows that the predicted curve of the present model is always above that of Sassa and Sekiguchi (2001) before χ_0 = 0.14. One possible reason for this difference (as mentioned above) is that the present model considers the effect of σ'_y whereas Sassa and Sekiguchi's model does not. Moreover, the present model assumes PSR can independently generate plastic strain and relates the normalized loading direction and plastic flow direction to the stress tensor invariants, but not to the angle of PSR as suggested by Sassa and Sekiguchi (2001). Finally, the difference in adopted governing equations (quasi-static model for Sassa and Sekiguchi (2001) and *u-p* model for the present model) could also cause this

ACCEPTED MANUSCRIPT

minor discrepancy in the predicted results. For a comprehensive description of inertia terms and effects for different wave and soil conditions, refer to Jeng and Cha (2003) and Ulker et al. (2009). When $\chi_0 \geq 0.14$, the predicted curve of Sassa and Sekiguchi (2001) begins to exceed that of the present model. This is due to the use of different criteria for judging liquefaction in this study ($p_{\max} = 0.86|\sigma'_{v0}|$) (Ye et al. 2015) compared to that of Sassa and Sekiguchi (2001)($p_{\max} = 0.95|\sigma'_{v0}|$), which will be discussed later in further detail. Overall, the soil responses under wave loading simulated by the present model are in qualitative agreement with those predicted by Sassa and Sekiguchi (2001).

5. Application

The behaviors of marine sediment under storm wave loading are critical to the stability of the seafloor. In light of the random character of the real storm (Fig. 1), the JONSWAP spectrum is firstly adopted to simulate the storm (Franco et al. 1998). Then, the effects of PSR on storm wave-induced soil response are investigated and the effects of wave are also discussed by comparing the random wave with the representative regular wave. Finally, a parametric study is carried out to examine the effects of soil parameters on seabed liquefaction.

5.1. Generation of the Storm Wave

The best method to obtain a realistic simulation of the real storm wave loads is to incorporate all the frequency components and then to reproduce several hours of a random wave in real time. However, this is a computationally time-consuming process because only a few of the waves in each time series can produce extreme results. Thus, a shorter time period

ACCEPTED MANUSCRIPT

with a logical combination of crest elevations is more appropriate for simulating the extreme response for expected wave size within the sea state. In this study, the profile of random sea waves is considered to be a stationary stochastic process that follows the Gaussian (normal) distribution as suggested by Liu and Jeng (2007). For the sake of simplicity, the wave profile or the water surface elevation $\eta(x,t)$ can be represented by a finite number (M) of cosine wave components as follows (Longuet-Higgins 1957):

$$\eta(x,t) = \sum_{i=1}^{\infty} H_i \cos\left(k_i x - 2\pi \tilde{f}_i t + \varepsilon_i\right) \approx \sum_{i=1}^{M} H_i \cos\left(k_i x - 2\pi \tilde{f}_i t + \varepsilon_i\right) \quad (32)$$

where M is the total number of the single wave, which composes the random wave; H_i is the amplitude of the component wave in the i-th frequency; $\tilde{f}_i$ is the i-th representative frequency which is evenly distributed in the range of (f_{i-1}, f_i); ε_i is a random initial phase angle, which is evenly distributed in the range of (0, 2π); and k_i is the wave number of the i-th component, which can be determined from the following dispersion relationship:

$$\left(2\pi \tilde{f}_i\right)^2 = \mathrm{g} k_i \tanh(k_i d) \quad (33)$$

where g is the gravitational acceleration and d is the water depth.

The component wave amplitude H_i can be determined from a given function of the frequency spectrum $S(f)$ by

$$H_i = \sqrt{2S\left(\hat{f}_i\right) \Delta f_i},\ \hat{f}_i = (f_i + f_{i-1})/2\ ,\ \Delta f_i = f_i - f_{i-1} \quad (34)$$

In this study, the JONSWAP spectrum is used for frequency spectrum $S(f)$, as follows:

$$S(f) = \beta_j H_{1/3}^2 T_p^{-4} f^{-5} \exp\left[-\frac{5}{4}\left(T_p f\right)^{-4}\right] \gamma^{\exp\left[-\left(T_p f - 1\right)^2 / 2\sigma^2\right]} \quad (35)$$

where

$$\beta_j = \frac{0.0624[1.094 - 0.01915 \ln\gamma]}{0.23 + 0.0336\gamma - 0.185(1.9+\gamma)^{-1}},\ T_p = \frac{T_{1/3}}{[1 - 0.132(\gamma+2)^{-0.559}]}, \gamma \in [1,7], \sigma = \begin{cases} 0.07, & f \le f_p \\ 0.09, & f > f_p \end{cases} \quad (36)$$

ACCEPTED MANUSCRIPT

where T_p is the wave period corresponding to the frequency f_p at the spectral peak and γ is the peak enhancement factor that controls the sharpness of the spectral peak in the JONSWAP spectrum. In this study, γ is assumed to be 3.3 as suggested by Liu and Jeng (2007).

Considering the wave energy is mainly concentrated around the peak frequency, we set the frequency range from f_L (= 0) to f_H (= 5f_p) as discussed by Goda (2000). Then, we assumed that the frequency is equally divided in the range [f_L, f_H] by

$$\Delta f = \frac{f_H - f_L}{M} \quad (37)$$

Hence, the whole frequency domain is equally divided into [f_L, f_L+Δf], [f_L+Δf, f_L+2Δf]…[f_H−Δf, f_H]. The i-th representative frequency, $\tilde{f}_i$, can be randomly generated in the range of [f_{i-1}, f_i]. In addition, using Eq.(34), the corresponding i-th component wave amplitude H_i can be determined. Hence, the time history of random wave surface elevations can be obtained from Eq. (32).

In the present study, the real storm (d = 20 m, $H_{1/3}$ = 4 m, T_p = 11.8 s) with no wind and currents recorded by Franco et al. (1998) is simulated by adopting the JONSWAP spectrum with M = 100. A recording length of about 20 min is used, which includes about 100 consecutive waves to ensure that the sampling variability of the characteristic wave heights and periods are below an acceptable level. The data sampling interval is set to be 1 s, which is 1/10–1/20 of the significant wave period as recommended by Goda (2000). Fig. 6 illustrates the time history of the water surface elevation $\eta(x,t)$ at the fixed points x = 0 m, x = 150 m, and x = 300 m. It can be clearly observed that the water surface shows irregular fluctuation around the zero level due to wave randomness. Moreover, there is little difference in the distribution of η along the extension direction of the seabed.

ACCEPTED MANUSCRIPT

The comparison between the predicted and targeted frequency spectrum is an efficient method to validate the simulated random wave profiles. As shown in Fig. 7, the predicted spectrum is based on the simulated data of the wave profile (Fig. 6) by using the autocorrelation method and hamming window function. Both the target spectra and simulated spectra show that the wave energy concentrates around the peak frequency $f_p = 1/T_p = 0.085$ Hz, which is very close to the frequency corresponding to the significant wave period (i.e. $f_{1/3} = 1/T_{1/3} = 0.09$ Hz). Moreover, both the profile and magnitude of the target spectrum can be captured by the present predicted spectrum despite some underestimation around the maximum spectra value. Therefore, the simulation of the random wave is generally effective and can be used in analyzing the dynamic response of the seabed under a storm.

Based on tiihe aforementioned spectra, the wave-induced dynamic water pressure at the mudline can be expressed as follows:

$$\begin{cases} \sigma'_z = \tau_{xz} = 0 \\ p = \sum_{i=1}^{M} p_b^{(i)} \cos\left(k_i x - 2\pi \tilde{f}_i t + \varepsilon_i\right) = \sum_{i=1}^{M} \frac{\gamma_w H_i \cos\left(k_i x - 2\pi \tilde{f}_i t + \varepsilon_i\right)}{\cosh(k_i d)} \end{cases} \quad \text{at} \quad z = 0 \tag{38}$$

5.2. Parameters of Sandy Seabed

The parameters for the sandy seabed considered in this study use the parameters of Nevada Sand, which are listed in Table 3 (determined by Zienkiewicz et al. (1998)). The saturation of seabed soil and initial void ratio are assumed to be 98% and 0.658, respectively. Three soil elements on the centerline (x = 150 m) with centroids at z/h = 0.1, 0.5, and 0.9 (marked as point A, B, and C, respectively, in Fig. 1) are taken as representative points to understand the dynamics of a sandy seabed under a storm.

The initial conditions are determined from a pre-consolidation analysis for the seabed

ACCEPTED MANUSCRIPT

foundation under gravitational forces. Tension is considered to be positive. The stress state in the final consolidation state is taken as the initial condition in the following dynamic analysis. To further demonstrate the effects of PSR on the wave-induced soil response, the simulated results from the original PZIII model are also incorporated into the analysis for comparison.

5.3. Results and Discussion

5.3.1. Storm Wave-Induced Soil Response

An understanding of the stress state and associated excess pore pressure conditions are critical to predicting engineering behavior. Fig. 8 shows the time history of pore water pressure, vertical effective stress (σ'_z), and plastic volumetric strain (ε_v^p) at three typical buried depths on the centerline over the first 17 wave cycles. Corresponding with the random wave characteristics of the real storm wave, it can be seen that loading the excess pore pressure (p_e) at all typical monitored points results in irregular distribution with increasing cyclic repetition. Moreover, there is an associated sharp increase in the cyclic amplitude of p_e during the severest wave loading with the time range [$10T_p$, $12T_p$]. However, the difference in the response of residual pore pressure ($p_e^{(2)} = \int_t^{t+T} p_e dt/T$) during this time range is distinct at different buried depths. At shallower depths (e.g., Location A with $|z/h| = 0.1$ in Fig. 1), $p_e^{(2)}$ behaves as a constant because the associated soil becomes liquefied as early as $8T_p$ with σ'_z approaching zero and a sharp increase in ε_v^p. However, at greater depths (e.g., Locations B and C with $|z/h| = 0.5$ and 0.9 in Fig. 1, respectively) $p_e^{(2)}$ shows an associated significant increase during the severest storm wave loading. The corresponding σ'_z and ε_v^p experience a sharp decrease and increase, respectively. Thus, the existence of extreme storm wave loading accelerates soil liquefaction, which may be the main reason that offshore

ACCEPTED MANUSCRIPT

installations easily destabilize during storms (Christian et al. 1974; Herbich et al. 1984). Moreover, the cyclic amplitude of p_e is (unsurprisingly) negatively correlated with the buried depth because the transmission of wave loading always shows progressive attenuation along the buried depth of the seabed. However, as anticipated, the $p_e^{(2)}$ is more likely to build up in greater depths ($|z/h|$= 0.5 or 0.9) due to the fact that pore water near the seabed surface can drain out from the soil and is therefore less likely to build up in this region. The results also indicate that the developed model is capable of reproducing the elastoplastic behavior of a sandy seabed under storm wave loading involving the rotation of principal stress axes. In addition, the discrepancy in the accumulation of $p_e^{(2)}$ predicted by the present model and the original PZIII model is significant at the three monitored points, indicating that ignoring the effects of PSR will significantly underestimate the build-up of pore pressure and reduction of vertical effective stress in the seabed foundation, which could then lead to unsafe design in the construction of offshore structures.

Distribution of dynamic pore pressure is important in improving the understanding of PSR's effects on the response of a sandy seabed to storm waves. Snapshots of dynamic pore pressure at times $t = 5T_p$ and $t = 15T_p$ predicted by the present model and the original PZIII model are shown in Fig. 9. It can be clearly observed that pore pressures in a sandy seabed are not uniform, but fluctuate with vibrations at shallow depths. Moreover, it is clear that the dynamic pore pressures predicted by the present model are always greater than those predicted by the original PZIII model, including at times $t = 5T_p$ and $t = 15T_p$. PSR has a significant effect on the distribution of dynamic pore pressure in a sandy seabed.

Stress paths are another way to characterize the liquefaction susceptibility of the seabed

ACCEPTED MANUSCRIPT

under cyclic waves. Fig. 10 clearly shows the effective stress paths at three monitored points on the seabed foundation under storm waves. Near the surface of the seabed (e.g., Location A), there is a high rate of decrease in p' and q predicted by the present model with p' ultimately approaching zero, indicating that the associated soil becomes liquefied. Similar trends can be observed at a middle-buried depth (Location B) predicted by the present model. However, some distinctions exist between the effective stress paths of Locations A and B, as shown in Fig. 10. For Location A, q always shows a decrease with the reduction of p' until liquefaction. However, q at Location B firstly decreases, then shows a significant increase when p' approximately reduces to -20 kPa, then begins to decrease again with p' approaching -15kPa. This can be attributed to the different responses in shear stress (τ_{xz}) during the severest storm wave loading as shown in Fig. 10. It can be seen that there is little difference in τ_{xz} predicted by both models except at Location A. By examining the distribution of τ_{xz} at Location A, good agreement between τ_{xz} predicted by the present model and the original PZIII model during the first $8T_p$ can be observed. After that, the soil is subjected to liquefaction in light of the present model and its corresponding shear stress reduces significantly due to loss of shearing resistance. Thus, τ_{xz} will not be able to differentiate whether the wave height is large or small once the soil is liquefied. However, the soil at Location B is far from liquefaction during this period and its associated τ_{xz} shows a sharp fluctuation, which results in a significant fluctuation in the effective stress path because of extreme storm wave loading. Here, it is worth noting that the shear stress should theoretically be zero once the soil becomes liquefied. However, if this is calculated strictly in the present FEM program, the calculation will terminate due to a numerical error. Therefore, some

ACCEPTED MANUSCRIPT

special measures are utilized in this study to ensure that the program continues to investigate progressive liquefaction along the depth under storm loading. This may lead to the fluctuation of τ_{xz} around zero after liquefaction as shown in Fig. 10. In addition, Fig. 10 clearly displays that the sandy seabed at all monitored points is far from liquefaction, with p' being greater than zero, as predicted by the original PZIII model during the entire process. Thus, the effect of PSR is visible in the marked reduction in the mean effective stress.

Fig. 10 also clearly shows that the deviatoric stress paths predicted by the two models are a series of smooth ellipses with unequal long radii under the storm wave loading. Moreover, the tendency for progressive liquefaction can also be anticipated ($\sigma'_z = \sigma'_x$) ultimately due to the remarkable decrease in the deviatoric stress. However, the reduction speed predicted by the present model (shown by the blue solid line) is always higher than the simulated results of the original PZIII model (shown by the red dashed line). In addition, there exists a sharp increase in the long radius of the elliptic deviatoric stress path (except at Location A) predicted by the present model. This is due to the fact that the severest wave loading will lead to a significant fluctuation in the shear stress of non-liquefied soil, as shown in Fig. 10. Thus, the elliptic deviatoric stress path will correspondingly show an evident increase in the long radius.

As introduced previously, the angle of orientation (ψ) is a key parameter for differentiating the present model and the original PZIII in terms of PSR-induced shear deformations. The effects of PSR on the storm wave-induced soil response are somewhat reflected by ψ over time, as shown in Fig. 10. It is found that the discrepancy between the two models is considerably more obvious especially at shallower locations where the

ACCEPTED MANUSCRIPT

wave-induced shear strain is significant. The amplitude of ψ predicted by the present model shows a more significant increase compared to the original PZIII, which in turn affects plastic soil deformation and the subsequent build-up of pore pressure. The results further confirm that ignoring PSR-induced deformations will significantly underestimate the instability of soil under storm waves.

5.3.2. Progressive Liquefaction

When a sandy seabed is exposed to storm waves, the bed soil will undergo periodic, elastoplastic, and shear deformation, which gradually rearranges the soil grains at the expense of pore volume. Presumably, pore pressure tends to progressively accumulate when the drainage condition is impeded and will significantly increase in the case of the severest storm wave loading. If the accumulated pore pressure exceeds the overburden pressure, the soil may even be liquefied, whereby the soil grains become unbounded and completely free, and the soil starts to behave like a liquid. To better address the liquefaction mechanism of a sandy seabed under storm wave loading, the parameter L_{p} (residual liquefaction potential) is defined as follows:

$$L_p = \left|\frac{\sigma'_{zd}}{\sigma'_{z0}}\right| \quad (39)$$

where $\sigma'_{zd} = (\sigma'_z - \sigma'_{z0})$ is the wave-induced vertical effective stress and σ'_z and σ'_{z0} are the current and initial effective stress, respectively.

Okusa (1985) proposed criteria for liquefaction, based on the vertical effective stress σ'_{z0} and σ'_{zd}:

$$|\sigma'_{zd}| = |\sigma'_{z0}| \quad (40)$$

According to Okusa's liquefaction criteria (Eq. (40)), the sandy soil becomes liquefied

ACCEPTED MANUSCRIPT

only when L_p is equal to or greater than 1.0. However, the value of L_p in sandy soil cannot exceed 1.0 in practical laboratory tests (Wu et al. 2004) or numerical simulations (Ye et al. 2015) because the sandy soil lacks cohesion and cannot withstand tensile stress unlike silty or clay soil. Then, Wu et al. (2004) suggested that sandy soil could be considered to be liquefied when $L_p \geq 0.78$–0.99. In this study, the Nevada medium-dense sand is considered to be liquefied when $L_p \geq 0.86$ (Ye et al. 2015).

The vertical distribution of accumulated pore water pressure at different times is shown in Fig. 11, where L_r represents the liquefaction resistance line of sandy soil, which is equal to $0.86|\sigma'_{z0}|$. As seen in Fig. 11, $p_e^{(2)}$ increases with increasing wave repetitions and approaches the liquefaction resistance line but is incapable of exceeding it. Liquefaction occurs when $p_e^{(2)} = L_r$. The depth at which the residual pore pressure reaches L_r increases over time. However, the increased amplitude of liquefied depth is uneven over the same time interval. In particular, there exists a sharp increase during the time range [$10T_p$, $12T_p$] with the severest storm wave loading. The liquefaction potential also reflects significant differences between the present model and the original PZIII. The main reason for this is the omission of PSR-induced deformation in the original PZIII, which can significantly overestimate the liquefaction resistance of a sandy seabed, leading to unsafe design in engineering practice.

5.3.3. Storm Wave-Induced Liquefaction Depth of a Sandy Seabed along the Extension Direction of the Seabed

The earlier discussions have mainly focused on storm wave-induced soil response on the centerline of the seabed. As shown in Fig. 9, there still exists a small difference in the water

ACCEPTED MANUSCRIPT

surface elevation (η) along the wave propagation direction due to the random characteristics of the storm. Thus, it is necessary to investigate the progressive liquefaction process along the extension direction of the seabed. Here, the gradual increase in liquefaction depth at x = 50 m, 100 m, 200 m, and 250 m predicted by the present model are shown in Fig. 12. The corresponding results at the centerline are also included in Fig. 12 for comparison. It is clearly seen that there is good agreement between each of the five liquefaction depth lines. Thus, it can be concluded that there is little discrepancy in the soil response during the storm along the extension direction of the seabed. This is because the random wave retains the moveable characteristics of the regular progressive wave, which results in similar cyclic loading along the random wave propagation direction.

5.3.4. Comparison of the Random Wave and Regular Wave

In this section, the difference in dynamic response of the seabed between the random wave and its representative regular wave is further investigated using the developed model. As suggested by Sumer et al. (1999), the parameters $H_r = H_{1/3}/\sqrt{2}$ and $T_r = \bar{T}$ are used to model the wave height and wave period of the representative regular wave as they showed the best agreement with the random wave during the process of pore pressure build-up. $\bar{T}$ represents the mean zero upcrossing period of a random wave record, which can be determined as follows (Goda 2000):

$$\bar{T} = \sqrt{\frac{m_0}{m_2}}, m_0 = \int_0^\infty S(f)df, m_2 = \int_0^\infty f^2 S(f)df \quad (41)$$

where m_0 and m_2 are the 0-th and 2-th spectral moments, respectively.

In the computation, the seabed is considered to consist of Nevada Sand (Zienkiewicz et al. 1999) as parameterized in Table 3. The parameters for the random wave are T_p=11.8 s,

ACCEPTED MANUSCRIPT

$H_{1/3}$=4.0 m and the representative parameters for the regular wave are T_r =9.28 s, H_r = 2.83 m. Moreover, the water depth d=20m and the thickness of the seabed h=20 m.

Fig. 13 shows snapshots of liquefaction depths for different types of waves at time t = 5T_r and t = 15T_r. As anticipated, no significant differences in the horizontal distribution of the liquefaction depth can be observed. This case occurs regardless of whether under a random wave or regular wave, which is likely attributable to the moveable nature of both waves. It can also be clearly observed that the development of the liquefied depth under the random wave is far behind that under the representative regular wave. Over the first five T_r, no liquefaction can be observed across the entire depth of the sandy seabed under later wave loading. However, the liquefaction depth reaches 2 m under the regular wave during these periods. At 15 T_r, it approaches 11.5 m for the regular wave, exceeding the 6.5 m recorded for the random wave.

As displayed in Fig. 14, the development of residual pore pressure $p_e^{(2)}$ under both random and regular wave loadings show a hump-shaped distribution along the buried depth, in which the hump of $p_e^{(2)} = \left(p_{e,\max}^{(2)}\right)$ progressively moves down with an increase in liquefied depth. It is also clearly seen that the potential of liquefaction under the representative regular wave is much stronger than that under the random wave. Moreover, $p_{e,\max}^{(2)}$ for the regular wave increases uniformly with the time interval of wave loading (= 2T_r as shown in Fig. 14) because of its constant wave characteristic. However, the increase of $p_{e,\max}^{(2)}$ is uneven for the random wave because of its irregularity in wave height and wave period. In particular, there exists a sharp increase in $p_{e,\max}^{(2)}$ during the time range [14T_r, 16T_r], which is approximately equal to [10T_p, 12T_p]. As shown in Fig. 8, during this time, the

ACCEPTED MANUSCRIPT

seabed at the centerline experiences the severest storm wave loading, and so the liquefied depth is significantly increased. As discussed above, in practice, it is more important to investigate the soil response during the storm by adopting the random wave rather than the representative regular wave, although adopting the latter is more conservative. This is due to the fact that the sharp weakening of soil in liquefaction resistance during a real wave storm cannot be captured using regular wave loading.

5.3.5. Parametric Studies

The effects of soil permeability (k_{s0}) and saturation (S_r) on the variation in depth of accumulated residual pore pressure $\left(p_e^{(2)}\right)$ on the centerline of the seabed (x = 150 m) is also investigated, as shown in Fig. 15. It can clearly be seen that both the permeability and saturation of soil have a significant influence on the accumulation of residual pore pressure for sandy soil. It seems that residual pore pressure is difficult to accumulate in a very loose seabed when the initial permeability efficient k_{s0} is greater than 5.65×10^{-2} m/s due to the rapid dissipation of pore pressure. Then, the accumulated speed of $p_e^{(2)}$ increases with the deduction of k_{s0}. However, the difference is negligible when k_{s0} is less than 5.65×10^{-5} m/s. Therefore, the influence of k_{s0} on the build-up of residual pore pressure for sandy soil is limited to a certain range. In addition, the accumulation of $p_e^{(2)}$ is positively related to the saturation of sandy soil. This is due to the fact that the pure fluid in unsaturated sandy soil always performances significant compressibility because of its gas content.

6. Conclusions

Soil liquefaction in a sandy seabed under random waves has become a concern due to

ACCEPTED MANUSCRIPT

high instability of the seabed during the storm. As one of the most important characteristics of the dynamic response of soil under cyclic wave loading, the effect of PSR should be considered in the numerical analysis of the wave–seabed interactions. In this study, a modified version of PZIII considering the impact of PSR was proposed for investigating the stress–strain behavior of sandy soil under storm waves. The specific focus of this study is the effect of PSR on the potential of liquefaction involved in wave–seabed interactions. Based on the numerical examples, the following conclusions can be drawn:

(1) In the present model, the effect of PSR was treated as an additional item in the constitute relationship of soil. Moreover, the normalized loading and plastic flow directions are only dependent on the stress tensor invariants but not on the angle of principal stress rotation as suggested by Sassa and Sekiguchi (2001). The comparison results show that the simulated soil responses by the present model under cyclic loading are in qualitative agreement with experimental results.

(2) The soil response along the extension direction of the seabed between the random wave and its representative regular wave are almost identical because of the moveable characteristics of storm waves. The development of excess pore pressure, vertical effective stress, stress paths, cyclic mobility, and the angle of PSR in sandy deposits always show random characteristics that correspond with irregular storm wave loading. Moreover, the severest wave loading in a real storm will significantly magnify both the speed and extent of liquefaction of the sandy seabed, which may be the main reason offshore installations easily destabilize during storms (Christian et al. 1974; Herbich et al. 1984).

ACCEPTED MANUSCRIPT

(3) A large discrepancy in storm wave-induced soil response exists between the present model and the original PZIII model and the predicted results of the latter were found to be always less than those of the former. Thus, it is important to consider the effect of PSR in numerical analysis of wave–seabed interactions, otherwise the potential of liquefaction under cyclic wave loading in the sandy seabed will be significantly underestimated, which is extremely dangerous in practical coastal and offshore engineering.

(4) Comparison of the liquefaction potential of soil under the random wave and its representative regular wave shows that the latter produces a more conservative result. Unfortunately, the sharp weakening of soil in liquefaction resistance under the severest wave condition cannot be captured by it. It is suggested that random wave loading rather than representative regular wave loading be adopted to practically investigate soil response during storm.

(5) Parametric studies indicate that the properties of soil have a remarkable influence on the liquefaction depth of sandy soil. In short, liquefaction is more likely to be observed in a fully saturated soil when the drainage condition is impeded.

Acknowledgements

The National Nature Fund of China (Grant Nos. 51879133, 51409142, 41502285), the Nature Fund of Zhejiang Province (Grant No. LY17E080006), the China Postdoctoral Science Foundation Funded Project (Grant No. 2018M632221) and the Fundamental Research Funds for the Central Universities (Grant No. 2018B00514) are acknowledged for

ACCEPTED MANUSCRIPT

their financial support. This study was also sponsored by K.C. Wong Magna Fund in Ningbo University of China.

ACCEPTED MANUSCRIPT

ACCEPTED MANUSCRIPT

References

Biot, M.A., 1956. Theory of propagation of elastic waves in a fluid-saturated porous solid. I. low-frequency range. J. Acoust. Soc. Am. 28(2), 168-178.

Bretschneider, C.L., 1968. Significant waves and wave spectrum. Ocean Industry Feb. 40-46.

Chan, A.H.C., 1995. User manual for DIANA-SWANDYNE II, Department of Civil Engineering, Univ. of Birmingham.

Chen W Y, Chen G X, Chen W, Liao C.C., Gao, H.M. 2018. Numerical simulation of the nonlinear wave-induced dynamic response of anisotropic poro-elastoplastic seabed. Mar. Georesour. Geotec. 1-12.

Christian, J.T., Taylor, P.K., Yen, J.K.C., Erali, D.R., 1974. Large diameter underwater pipeline for nuclear plant designed against soil liquefaction. Offshore Technology Conference, May 6-8, 1974, Houston, TX, OTC 2094, 597-606.

Franco, L., de Gerloni, M., Passoni, G., Zacconi, D., 1998. Wave forces on solid and perforated caisson brekwaers: comparison of field of field and laboratory measurements. Coast. Eng. 1945-1958.

Goda, Y., 2000. Random seas and design of marine structures. World Scientific, Singapore.

Guo, Z., Jeng D.-S., Zhao, H. Y., Guo, W., Wang, L. Z. 2019, Effect of Seepage Flow on Sediment Incipient Motion around a Free Spanning Pipeline. Coastal Eng. 143, 50-62.

Hasselmann, K., Olbers, D., 1973. Measurements of wind-wave growth and swell decay during the Joint North Sea Wave Project (JONSWAP), Ergänzung zur Deut. Hydrogr. Z., Reihe A (8) 12, 1-95.

Herbich, J.B., Schiller, R.E., Dunlap, W.A., Watanabe, R.K., 1984. Seafloor Scour, Design Guidelines for Ocean-Founded Structures. Marcel Dekker.

Hunt, R.J., Marsh, P.D., 2004. Opportunities to improve the operational and technical management of

ACCEPTED MANUSCRIPT

jack-up deployments. Mar Struct., 17(3-4), 261-273.

Hsu, J.R.C., Jeng. D.-S., 1994. Wave-induced soil response in an unsaturated anisotropic seabed of finite thickness. Int J Numer Anal Met. 18(11),785-807.

Ishihara, K., Towhata, I., 1983. Sand response to cyclic rotation of principal stress directions as induced by wave loads. Soils Found. 23(4), 11-26.

Ishihara, K., Yamazaki, A., 1984. Analysis of wave-induced liquefaction in seabed deposit of sand. Soils Found. 24 (3), 85-100.

Jeng, D.-S., 2003. Wave-induced sea floor dynamics. Appl Mech Rev. 56(4), 407-429.

Jeng, D.-S., Cha, D. H., 2003. Effects of dynamic soil behavior and wave nonlinearity on the wave-induced pore pressure and effective stresses in porous seabed. Ocean Eng. 30, 2065-2089.

Jeng, D.S., Ou, J., 2010. 3-d models for wave-induced pore pressure near breakwater heads. Acta Mechanica 215(1-4), 85-104.

Jeng, D.-S, Seymour, B. R., 2007. A simplified analytical approximation for pore-water pressure build-up in a porous seabed. J. Waterway, Port, Coastal, Ocean Eng. ASCE. 133(4), 309-312.

Jeng, D.-S., Zhao, H. Y., 2015. Two-dimensional model for accumulation of pore pressure in marine sediments. J. Waterway, Port, Coastal, Ocean Eng., ASCE. 141(3), 1-12.

Kirca, V. S., Sumer, B. M., Fredsoe, J., 2013. Residual liquefaction of seabed under standing waves. J. Waterw. Port Coast. Ocean Eng. 139 (6), 489-501.

Li, K., Guo, Z., Wang, L. Z., Jiang, H.Y. 2019. Effect of Seepage Flow on Shields Number around a Fixed and Sagging Pipeline, Ocean Eng. 172(15), 487-500.

Li, H. E., He, Y. J., Fan, G. Y., Li, T. C., Pastor M., 2011. Recent development of generalized plasticity models for saturated and unsaturated soils. Water Science and Engineering. 4(3), 329-344.

ACCEPTED MANUSCRIPT

Liu, H. J., Jeng D. S., 2007. A semi-analytical solution for random wave-induced soil response and seabed liquefaction in marine sediments. Ocean Eng. 34, 1211-1224.

Liu, P, Wang, Z.T., Li, X.Z., Chan, A.H.C., 2015. Calibration and validation of a sand model considering the effects of wave-induced principal stress axes rotation. Acta Oceanology Sina. 34(7), 105-115.

Longuet-Higgins, M.S., 1957. The statistical analysis of a random, moving surface. Philosophical Transactions of the Royal Society of London, A. 249(966), 321-387.

Mitsuyasu, H., 1970. On the growth of spectrum of wind-generated waves(2) – spectral shape of wind waves at finite fetch. Proc. Japanese Conf. Coastal Engrg. 1-7.

Miyamoto, T., Yoshinaga, S., Soga, F., Shimizu, K., Kawamata, K., Sato, M., 1989. Seismic prospecting method applied to the detection of offshore breakwater units settling in the seabed. Coastal Eng. 32 (1), 103-112.

Miyamoto, J., Sassa, S., Sekiguchi, H., 2004. Progressive solidification of a liquefied sand layer during continued wave loading. Géotechnique, 54(10), 617-629.

Okusa, S., 1985. Wave-induced stress in unsaturated submarine sediments. Géotechnique. 35(4), 517-532.

Pastor, M., Zienkiewicz, O.C., Chan, A. H. C., 1990. Generalized plasticity and the modelling of soil behaviour. Int. J. Numer. Anal. Methods Geomech. 14, 151-190.

Pastor, M., Zienkiewicz, O. C., Li, T., Xiaoqing, L., Fernandez Merodo, J. A., Mira, P., 1999. Modelización del comportamiento sísmico de geoestructuras. Física de la Tierra. 11, 175-201.

Pan, K., Yang, Z. X., 2018. Undrained behavior of sand under cyclic paths that match storm-wave loading conditions. Mar. Georesour. Geotec. 36(1), 72-82.

Perić, D., Ayari, M. A., 2002. Influence of Lode's angle on the pore pressure generation in soils. Int. J. Plasticity. 18(8), 1039-1059.

ACCEPTED MANUSCRIPT

Pierson, W.J., Moskowitz, L., 1963. A proposed spectral form for fully developed wind seas based on the similarity theory of S. A. Kitaigorodskii.

Qian, J.G., Wang, Y.G., Yin, Z.Y., Huang, M.S., 2016. Experimental identification of plastic shakedown behavior of saturated clay subjected to traffic loading with principal stress rotation. Eng. Geol. 214, 29-42.

Sassa, S., Sekiguchi, H., 1999. Wave-induced liquefaction of beds of sand in a centrifuge. Géotechnique. 49(5), 621-638.

Sassa, S., Sekiguchi, H., 2001. Analysis of wave-induced liquefaction of sand beds. Géotechnique. 51(2), 115-126.

Sassa, S., Takayama, T., Mizutani, M., Tsujio, D., 2006. Field observations of the build- up and dissipation of residual pore pressures in seabed sands under the passage of storm waves. J. Coastal Res. 39, 410-414.

Sumer, B.M., Fredsøe, J., Christensen, S., Lind, M.T., 1999. Sinking/floatation of pipelines and other objects in liquefied soil under waves. Coastal Eng. 38, 53-90.

Symes, M. J. P. R., Gens, A., Hight, D. W., 1984. Undrained anisotropy and principal stress rotation in saturated sand. Géotechnique. 34(1), 11-27.

Towhata, I., Ishihara, K., 1985. Undrained strength of sand undergoing cyclic rotation of principal stress axes. Soils Found. 25(2), 135-147.

Ulker, M. B. C., Rahman, M., Jeng, D.-S., 2009. Wave-induced response of seabed: various formulations and their applicability. Appl. Ocean Res. 31, 12-24.

Wang, Z., Yang, Y. M., Yu, H. S., 2017a. Effects of principal stress rotation on the wave-seabed interactions. Acta Geotech. 12(1), 97-106.

ACCEPTED MANUSCRIPT

Wang, Z.T., Liu, P., Jeng, D.-S., Yang, Q., 2017b. Cyclic strength of sand under a nonstandard elliptical rotation stress path induced by wave loading. J. Hydrodyn. 29(1), 89-95.

Wu, J., Kammaerer, A. M., Riemer, M. F., Seed, R. B., Pestana, J. M., 2004. Laboratory study of liquefaction triggering criteria. In Proceedings of 13th World Conference on Earthquake Engineering, Vancouver, British Columbia, Canada. Paper No. 2580.

Xu, C.S., Jia, J.B., Sun, Y.L., Du, X.L., Gao Y., 2017. Cyclic strength of saturated sand under bi-directional cyclic loading. Eng. Geol. 227, 23-31.

Yang, Z. X, Li X. S., Yang, J., 2007. Undrained anisotropy and rotational shear in granular soil. Géotechnique. 57(4), 371-384.

Ye, J. H., Jeng, D.-S., Wang, R., Zhu, C. Q., 2015. Numerical simulation of wave-induced dynamic response of poro-elasto-plastic seabed foundation and composite breakwater. Appl. Math. Model. 39, 322-347.

Zhang, Y. Jeng, D.-S., Fu, Z. W., Ou, J., 2013. Random wave-induced seabed responses around breakwater heads. Geotechnical Engineering Journal of the SEAGS & AGSSEA. 44(3), 65-83.

Zhao, H.Y., Jeng, D.-S., Zhang, J.S., Liao, C.C., Zhang, H.J., Zhu, J.F., 2017a. Numerical study on loosely deposited foundation behavior around a composite breakwater subject to ocean wave impact. Eng. Geol. 227, 121-138.

Zhao, K., Xiong, H., Chen, G.X., Zhuang, H.Y., Du, X.L., 2017b. Cyclic characterization of wave-induced oscillatory and residual response of liquefiable seabed. Eng. Geol. 227, 32-42.

Zienkiewicz, O. C., Chan, A. H. C., Pastor. M., Schrefler, B. A., 1998. Computational geomechanics with special reference to earthquake engineering. John Wiley & Sons Ltd, England.

Zhou, X.L., Zhang, J., Guo, J.J., Xu, F., 2014. Numerical study for random wave-induced porous seabed

ACCEPTED MANUSCRIPT

response. International Conference on Civil Engineering, Energy and Environment, 21-25.

ACCEPTED MANUSCRIPT

ACCEPTED MANUSCRIPT

Table 1 Parameters in the present constitutive model used in the computation for HCA element test of sand (Sassa and Sekiguchi 2001)

Parameter	Value	Unit
K_{ev0}	2,4727.3	kPa
G_{ev0}	3,4000	kPa
p'_0	4.0	kPa
M_{g0}	0.7	-
M_{f0}	0.42	-
α_0	0.005	-
β_0	0.3	-
β_1	5.5	-
H_0	650	kPa
H_{u0}	1,000	kPa
γ_U	6.0	-
a	0.25	-
b	0.65	-

ACCEPTED MANUSCRIPT

ACCEPTED MANUSCRIPT

Table 2 Parameters used for comparison with the centrifugal test (Sassa and Sekiguchi 2001)

Type	Parameter	Value	Unit
Wave	T	4.55	/s
	d	4.5	/m
	H	1.7	/m
	L_0	25.5	/m
Seabed	W	10.0	/m
	h	5.0	/m
	S_r	100	/%
	k_s	1.5×10^{-4}	/(m·s^{-1})
PZIII model	K_{ev0}	1982.4	/kPa
	G_{ev0}	2100	/kPa
	β_0	0.2	-
	H_0	700	/kPa
	H_{u0}	1000	/kPa
	p'_0	4.0	/kPa
	γ_U	6.0	-
	n	0.48	-
	M_{g0}	0.7	-
	M_{f0}	0.42	-
	α_0	0.01	-
	K_0	0.52	-
	a	0.3	-
	b	0.5	-

ACCEPTED MANUSCRIPT

ACCEPTED MANUSCRIPT

Table 3 Parameters in the dynamic constitutive model used in computation for the sandy seabed

Item	Constitutive model		Unit
	Original PZIII	Present model	
K_{ev0}	2000	2000	kPa
G_{ev0}	2600	2600	kPa
p_0'	4.0	4.0	kPa
M_g	1.32	-	-
M_f	1.3	-	-
α_g	0.45	-	-
α_f	0.45	-	-
β_0	4.2	4.2	-
β_1	0.2	0.2	-
H_0	750	750	kPa
H_{u0}	40,000	40,000	kPa
γ_U	4.0	4.0	-
S_r	0.98	0.98	-
n	0.397	0.397	-
k_s	5.65×10^{-5}	5.65×10^{-5}	$m\cdot s^{-1}$
M_{g0}	-	1.32	-
M_{f0}	-	1.3	-
α_0	-	0.45	-
a	-	0.3	-
b	-	0.5	-

ACCEPTED MANUSCRIPT

ACCEPTED MANUSCRIPT

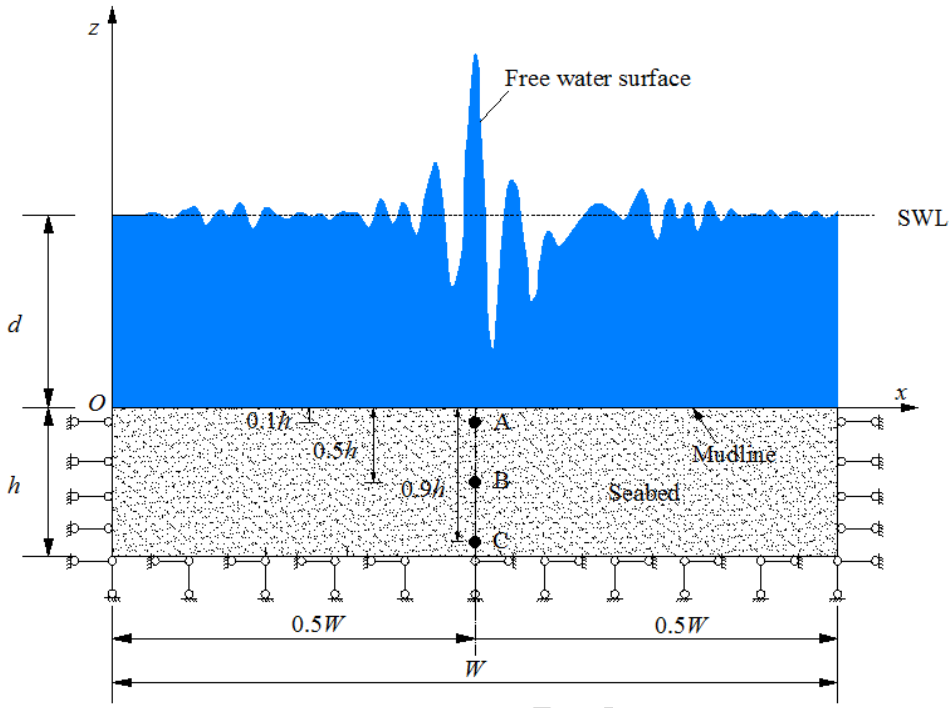

Fig. 1. Schematic of random wave system in a storm

ACCEPTED MANUSCRIPT

ACCEPTED MANUSCRIPT

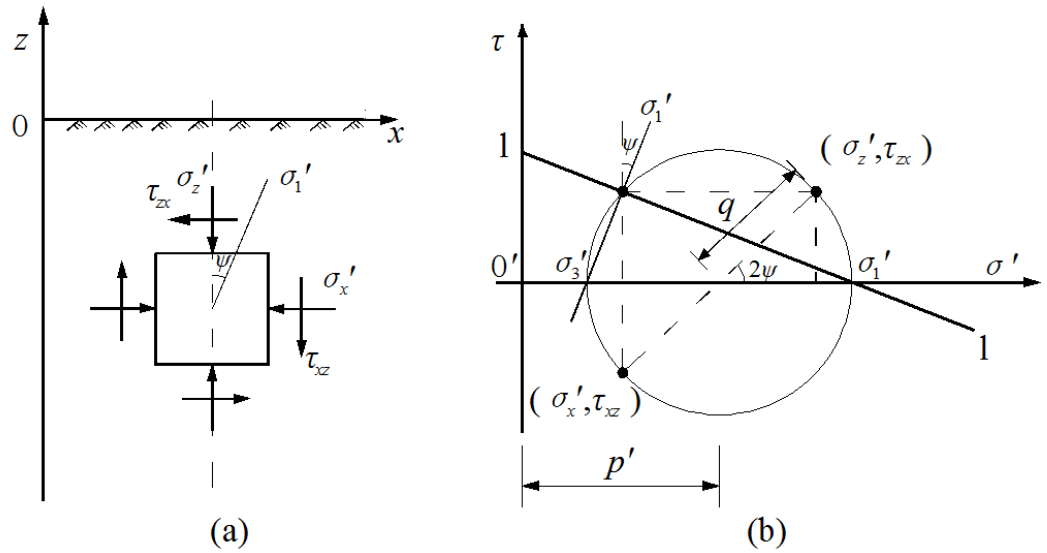

Fig. 2. Schematic of principal stress rotation under plain strain conditions (Sassa and Sekiguchi 2001)

ACCEPTED MANUSCRIPT

ACCEPTED MANUSCRIPT

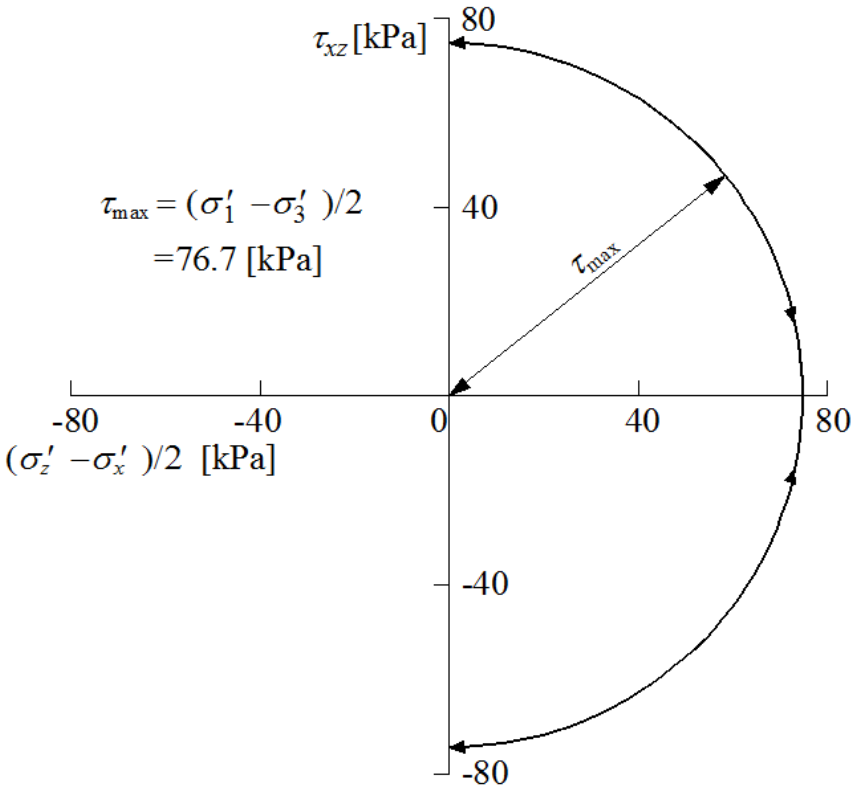

Fig. 3. Stress paths for HCA element test with fixed orientations of the major principal stress axes

(Towhata and Ishihara, 1985)

ACCEPTED MANUSCRIPT

ACCEPTED MANUSCRIPT

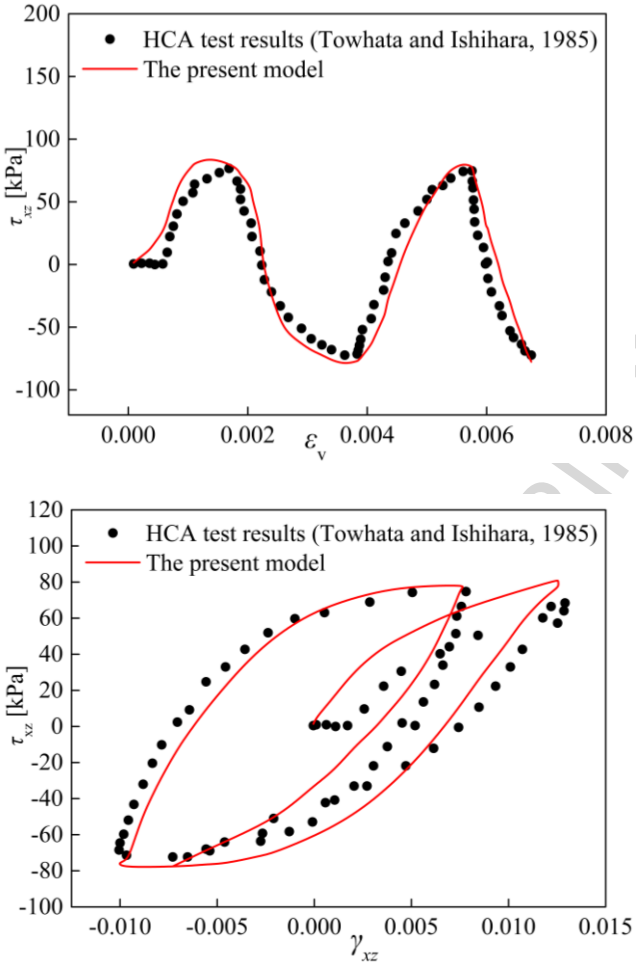

Fig. 4. Comparison of the present model with the HCA tests under continuous rotation of the major principal stress axis

ACCEPTED MANUSCRIPT

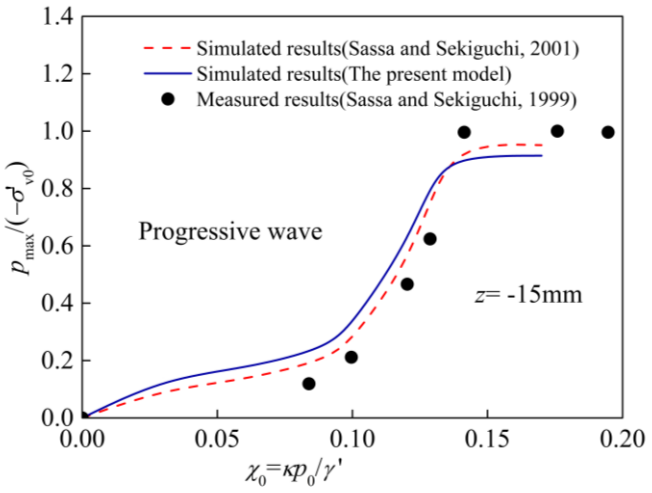

Fig. 5. Comparison of simulated results with centrifuge wave tests at shallow soil depth

ACCEPTED MANUSCRIPT

ACCEPTED MANUSCRIPT

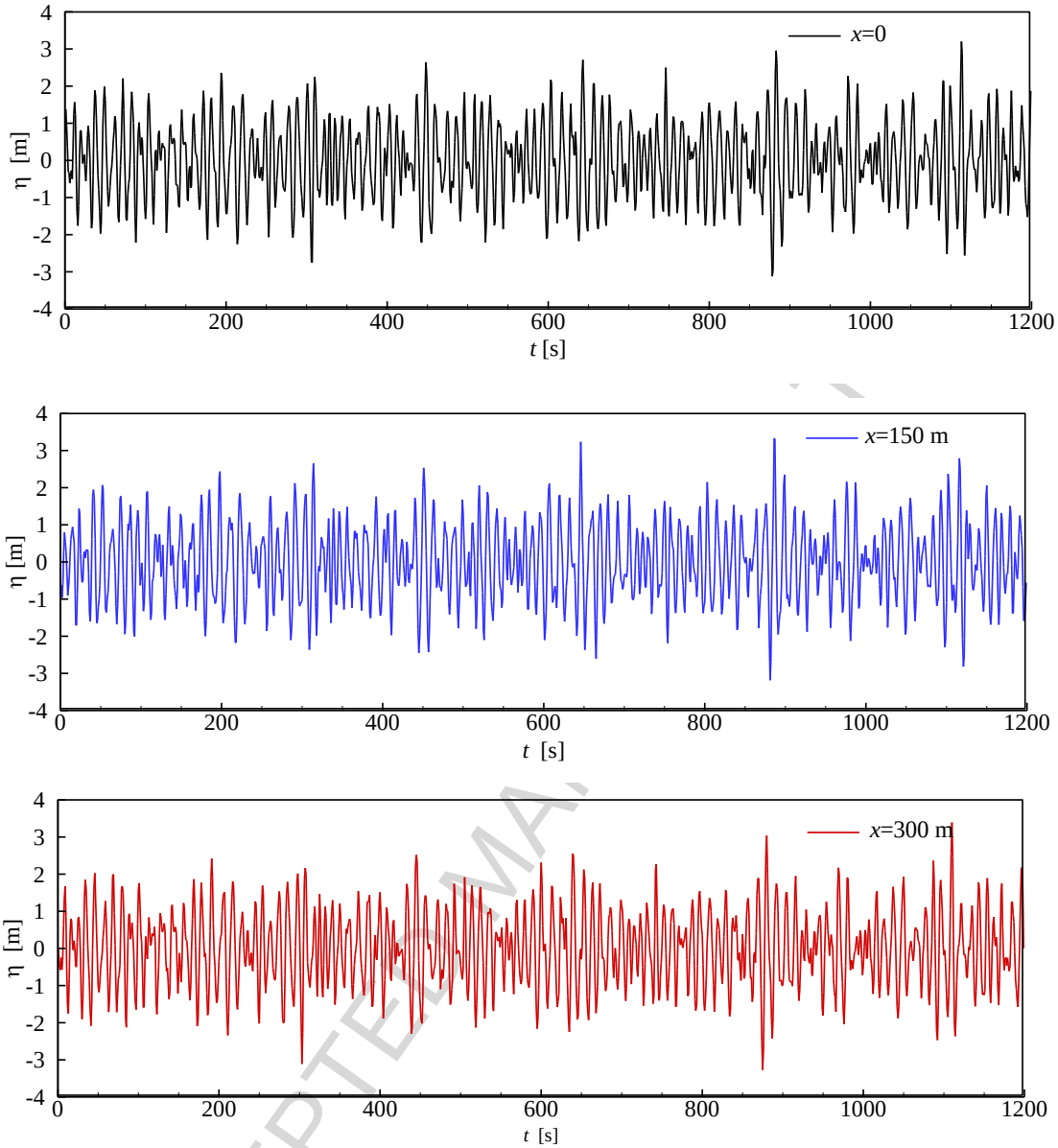

Fig. 6. Time history of simulated random wave profiles using JONSWAP spectrum

ACCEPTED MANUSCRIPT

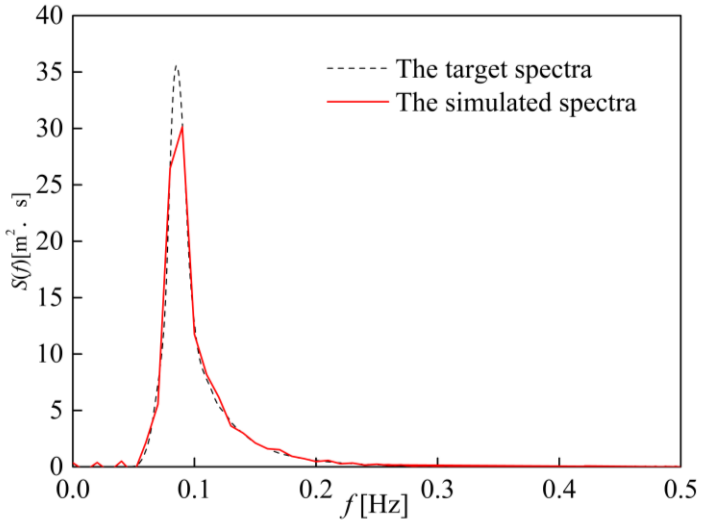

Fig. 7. Comparison of predicted spectrum (solid lines) and target spectrum (dashed lines) for JONSWAP spectrum

ACCEPTED MANUSCRIPT

ACCEPTED MANUSCRIPT

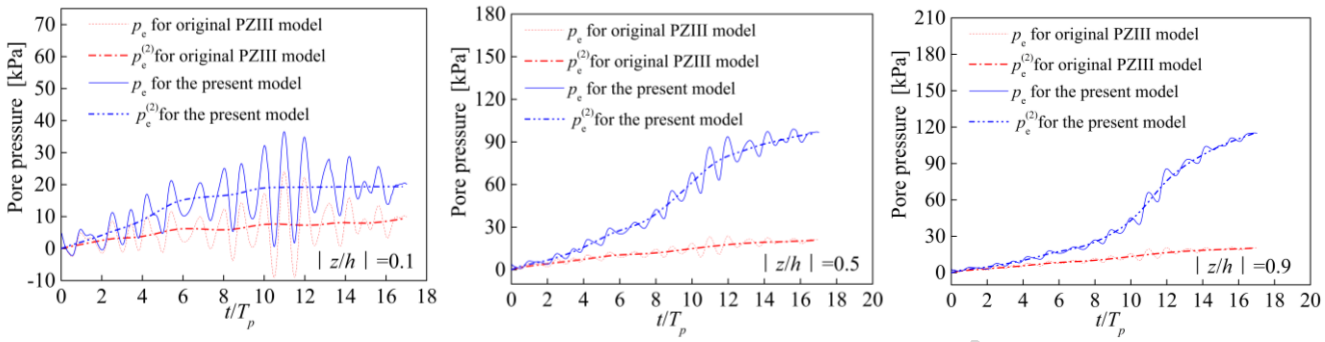

(a) Pore pressure at different depths

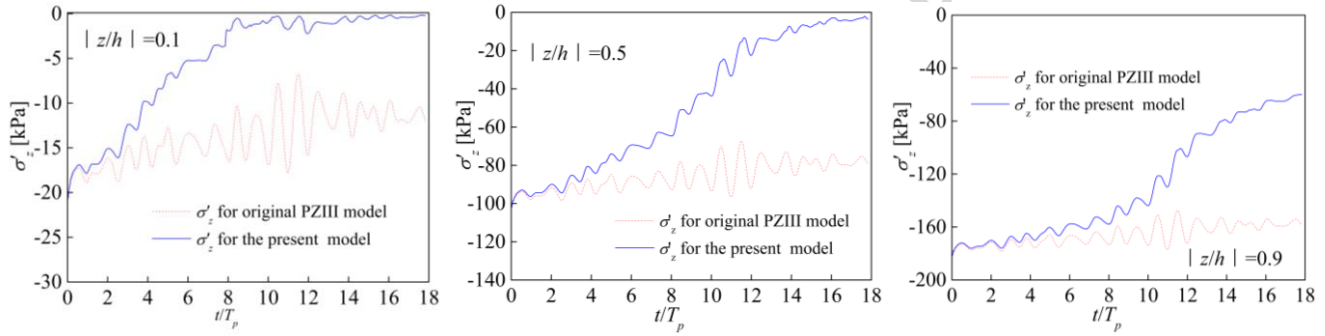

(b) The vertical effective stress at different depths

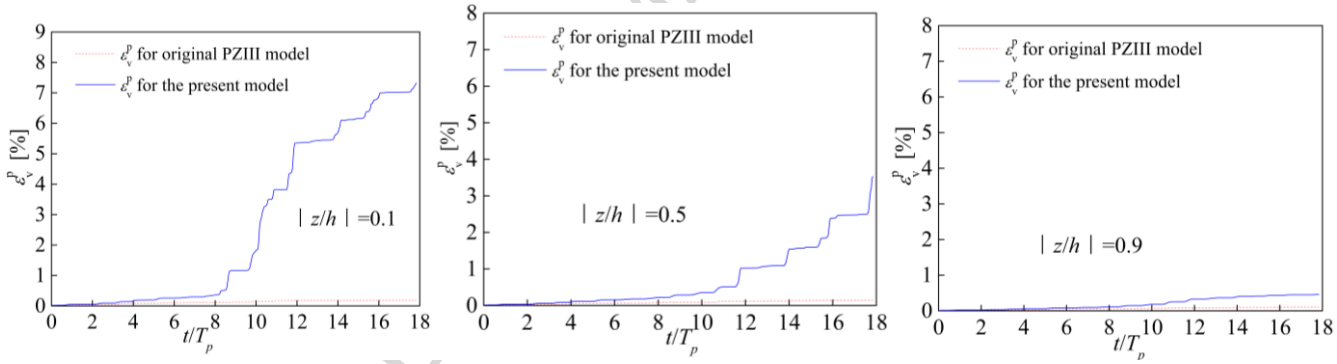

(c) The plastic volumetric strain at different depths

Fig. 8. Dynamic response on typical positions in the sandy seabed under random wave loading

ACCEPTED MANUSCRIPT

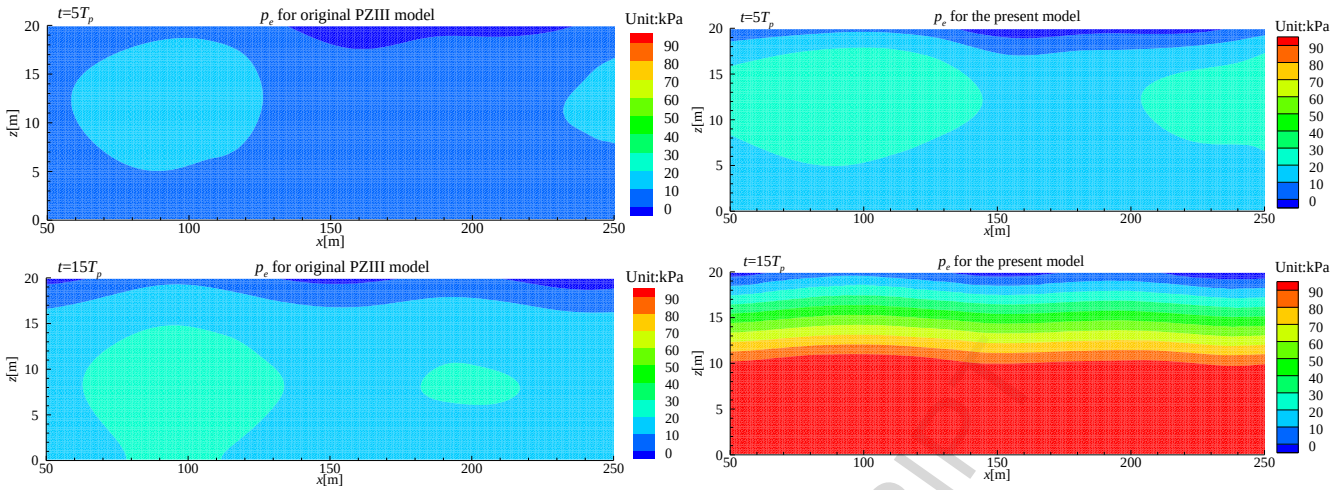

(a) The original PZIII model (b) The present model

Fig. 9. Distribution of random wave-induced excess pore pressure in sandy seabed at time $t/T_p = 5$ and $t/T_p = 15$

ACCEPTED MANUSCRIPT

ACCEPTED MANUSCRIPT

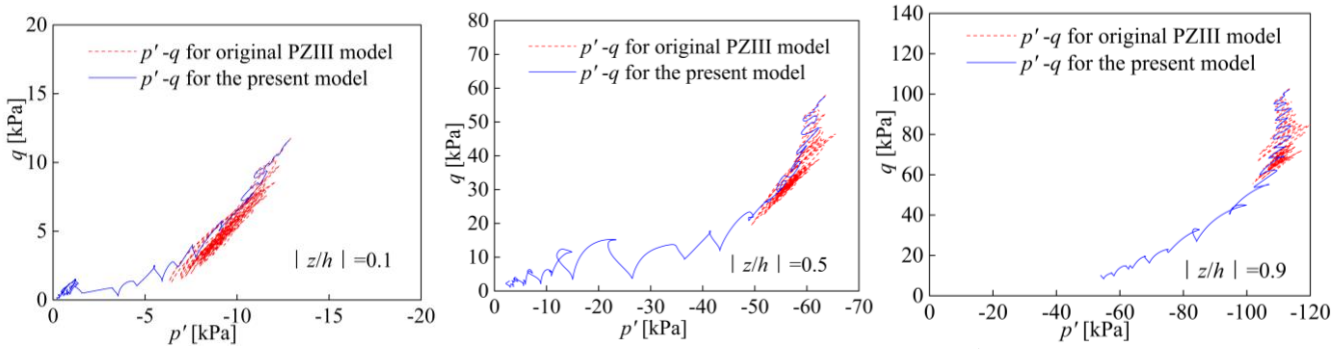

(a) Effective stress paths

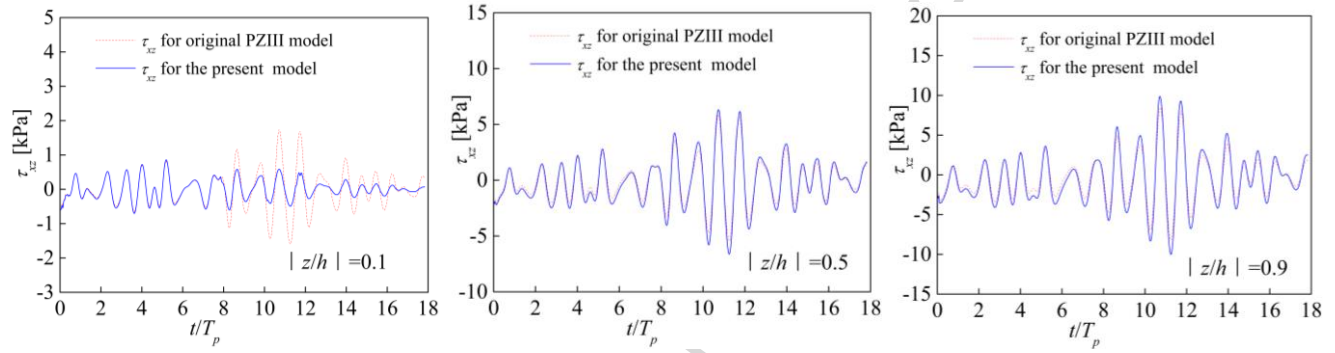

(b) Shear stress

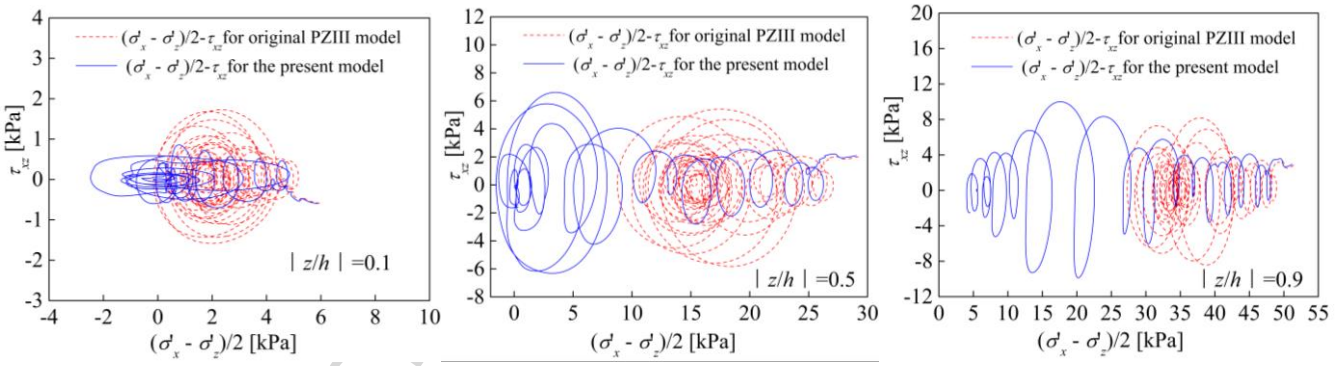

(c) Deviatoric stress paths

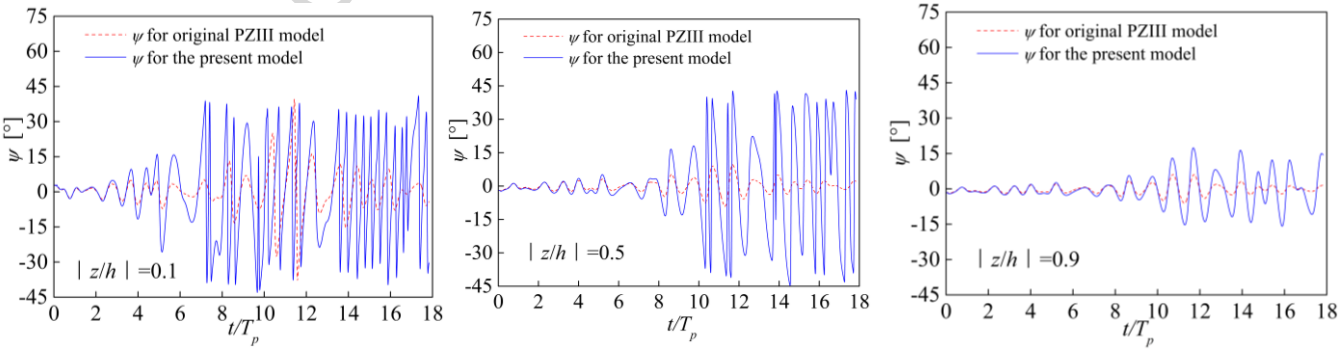

(d) Angle of orientation of the major principal stress axes to the vertical

Fig. 10. Stress paths, shear stress and angle of orientation on typical positions subjected to random wave loading

ACCEPTED MANUSCRIPT

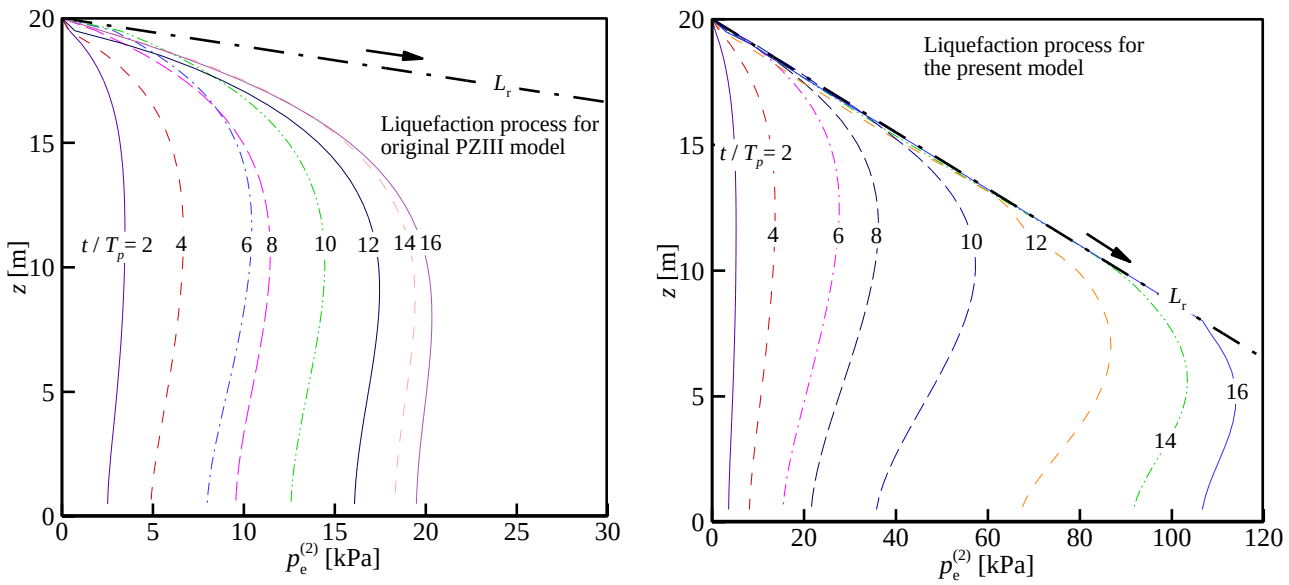

(a) The original PZIII model (b) The present model

Fig. 11. Vertical distribution of progressive wave-induced pore pressure

ACCEPTED MANUSCRIPT

ACCEPTED MANUSCRIPT

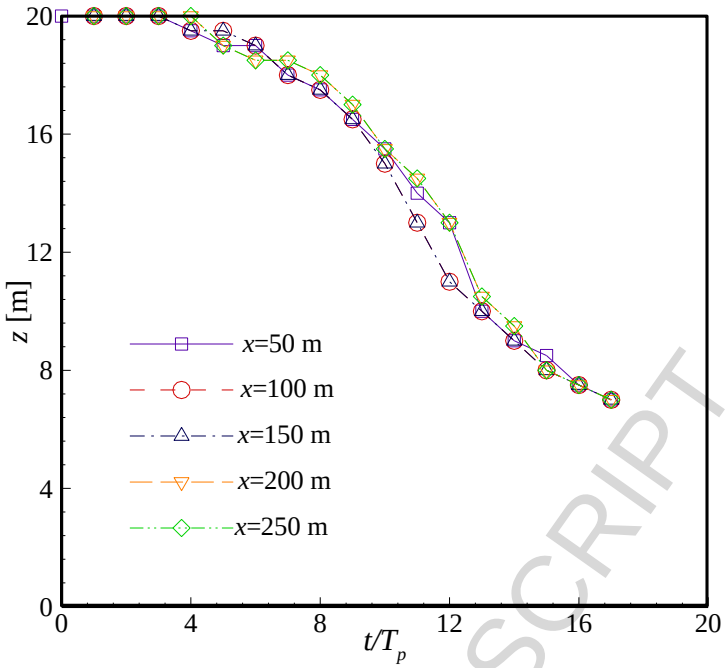

Fig. 12. Progressive liquefaction process along the extension direction of the seabed

ACCEPTED MANUSCRIPT

ACCEPTED MANUSCRIPT

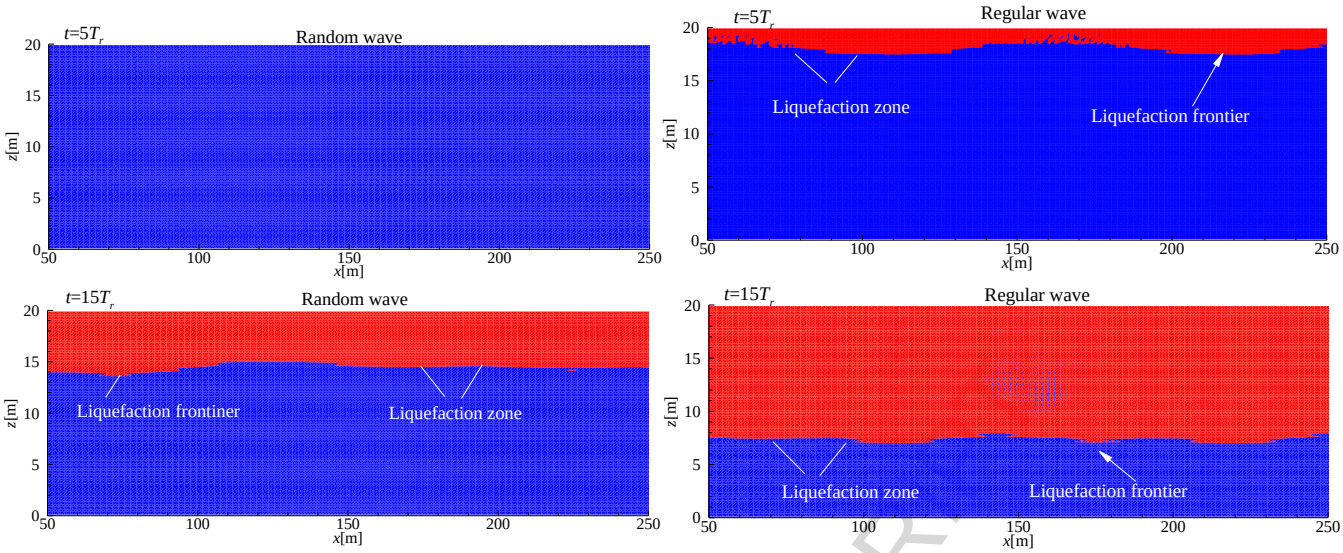

(a) Random wave (b) Regular wave

Fig. 13. Distribution of wave-induced dynamic pore pressure in sandy seabed at time $t/T_r = 5$ and $t/T_r = 15$

ACCEPTED MANUSCRIPT

ACCEPTED MANUSCRIPT

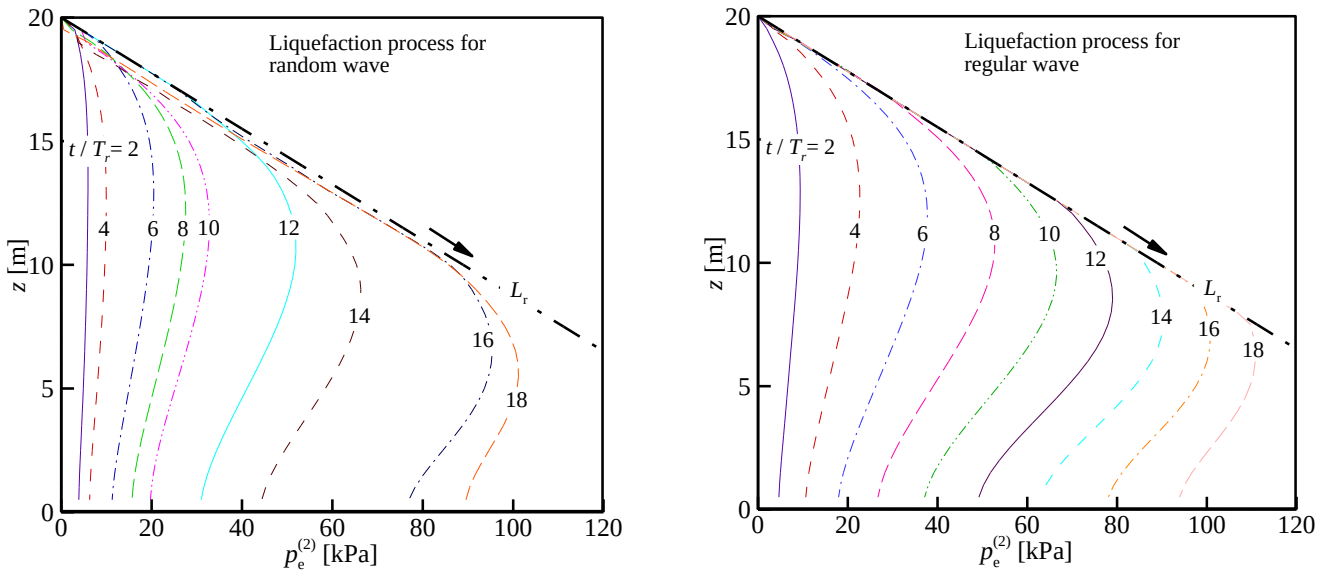

(a) The random wave (b) The regular wave

Fig. 14. Vertical distribution of progressive wave-induced pore pressure

ACCEPTED MANUSC

ACCEPTED MANUSCRIPT

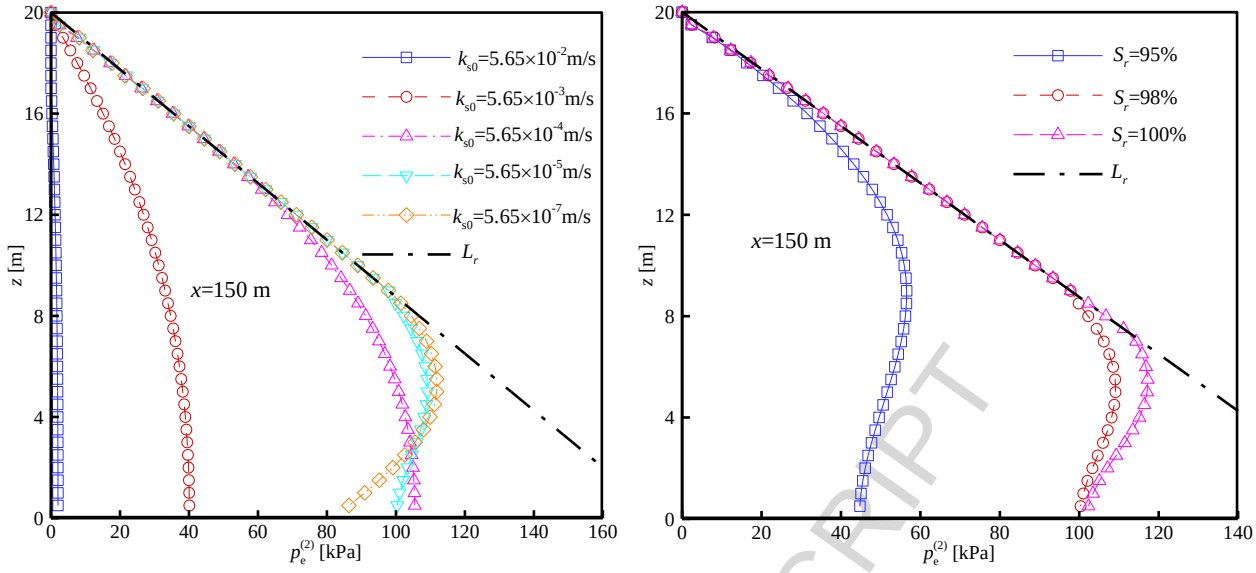

(a) Various k_{s0} (b) Various S_r

Fig. 15. Vertical distribution of accumulated residual pore pressure on centerline after 15 T_p for (a) various k_{s0} and (b) various S_r

ACCEPTED MANUSCRIPT

ACCEPTED MANUSCRIPT

Highlights

- A generalized plasticity model concerning the impact of principal stress rotation (PSR) in the seabed soil is developed.
- The cyclic behavior of elastoplastic seabed foundation during the storm wave loading is numerically investigated.
- The liquefaction resistance of sandy seabed is greatly affected by the loading irregularity and principal stress rotation.

ACCEPTED MANUSCRIPT